VIV analysis of a subsea power cable during installation in high current seas

D. F. Kallias Ntroumpis

Delft University of Technology

VIV analysis of a subsea power cable during installation in high current seas

by

D. F. Kallias Ntroumpis

to obtain the degree of Master of Science
at the Delft University of Technology,
to be defended publicly on Monday September 25, 2017 at 09:30 AM.

Student number:	4512863	
Project duration:	January 9, 2017 – September 25, 2017	
Thesis committee:	Prof. dr. A. Metrikine,	TU Delft, Chairman
	Ir. Y. Qu,	TU Delft, Supervisor
	Ir. C. Visser,	Tideway Offshore Solutions
	Ir. M. Hassan,	Tideway Offshore Solutions

This thesis is confidential and cannot be made public until September 25, 2022.

Abstract

During installation of subsea power cables in high ocean currents, significant vibrations might occur. These vibrations are called vortex induced vibrations (VIV) and they are result of the vortex shedding behind the cables. Significant forces may arise due to VIV which can compromise the cable's integrity limits and further introduce problems to the installation procedure. The main objective of this research is to assess the effects of the VIV on the cables and provide solutions to improve workability.

In this thesis a coupled wake-structure model was created in order to study the interaction between the vortices and the cable. The model is based on the phenomenological model of the wake oscillator which can capture well the self-exciting, self-limiting behavior of VIV, therefore estimating accurately enough the lock-in region and vibration amplitude. A wake oscillator with acceleration coupling is used and different sets of tuning parameters tuned to 1DOF and 2DOF free vibration experiments are examined. The structure has been modeled in the finite element software OrcaFlex and the wake oscillator model was implemented as an external function in the programming language Python.

To confirm the validity of the above mentioned model two experiments were used. Firstly, the model was tested against the Delft flume experiment where the case of a vertical riser is examined and further the São Paulo experiment where the case of a steel catenary riser (SCR) is studied. The model was also compared with the Milan wake oscillator model from OrcaFlex's VIV toolbox. The model showed good agreement with the experimental results and found to be superior of OrcaFlex's VIV model.

Next, VIV analysis was performed for a case study. The analysis was done for different current speeds and directions and the effects of the VIV on the tension and the bending radius of the cable were determined. For lower current velocities, lock-in response and standing waves along the cable were observed, while for higher velocities multifrequency response, beating behavior and traveling waves were observed.

An important conclusion of this research is that the coupled wake-structure model used in this thesis is suitable for assessing VIV effects on catenary shaped cables. Furthermore, the analysis showed that catenary shaped cables with remaining length on the seabed exhibit smaller crossflow vibration amplitudes than straight cylinders.

Preface

I would like to thank my supervisors in Tideway Offshore Solutions, ir. Connie Visser and ir. Mohamed Hassan for proposing such an interesting topic and their support during this thesis. Special thanks to Mohamed for his willingness to provide help. Also, many thanks to my colleagues in the engineering department of Tideway for our interesting conversations, working with them was a pleasure.

I would like also to thank my university supervisors, chairman of my graduation committee Prof. Andrei Metrikine, for his critical advice and comments, and the PhD candidate ir. Yang Qu for his support. I am very grateful to Yang for our regular discussions which helped me to gain a better understanding on VIV and improve the level of my work.

Finally, I would like to express my gratitude to my friends and family for their support along this thesis.

To the memory of my beloved uncle *Michail*

D. F. Kallias Ntroumpis
Delft, September 2017

Contents

List of Figures

List of Tables

Nomenclature

Acronyms

DOF	Degree of Freedom
EOM	Equation of Motion
FEM	Finite Element Method
IP	Independence Principle
MBR	Minimum Bending Radius
ODE	Ordinary Differential Equation
SD	Spectral Density
TDP	Touch Down Point
VIV	Vortex Induced Vibrations
WOM	Wake Oscillator Model

List of Symbols

ϵ	Tuning parameter	$[-]$
μ	Seabed friction coefficient	$[-]$
ν	Kinematic viscosity	$[m^2/s]$
ω_s	Natural frequency of the oscillator	$[rad/s]$
ρ_w	Water density	$[kg/m^3]$
θ	Inclination angle	$[degrees]$
ζ	Material damping	$[-]$
A	Tuning parameter	$[-]$
c	Damping coefficient	$[kg/s]$
C_α	Potential added mass coefficient	$[-]$
C_{Do}	Drag coefficient for stationary cylinder	$[-]$
C_{Lo}	Lift coefficient for stationary cylinder	$[-]$
C_{VX}	Coefficient of lateral force	$[-]$
C_{VY}	Coefficient of vertical force	$[-]$
D	Diameter	$[m]$

d	Waterdepth	$[m]$
E	Young's Modulus	$[Pa]$
F	External force	$[N]$
f_n	Natural frequency	$[Hz]$
f_s	Shedding frequency	$[Hz]$
k	Spring coefficient	$[N/m]$
L	Element length	$[m]$
m^*	Mass ratio	$[-]$
m_α	Added mass	$[kg]$
q	Wake variable	$[-]$
Re	Reynolds number	$[-]$
St	Strouhal number	$[-]$
T	Tension force	$[N]$
U	Relative velocity	$[m/s]$
V	Undisturbed flow velocity	$[m/s]$
V_r	Reduced Velocity	$[-]$

1

INTRODUCTION

1.1. Background

The last years the demand for renewable energy has rapidly increased as the results of the climate change are becoming more evident. In December 2015, at the Paris Climate Change Conference (COP21), 195 countries adopted the first-ever universal, legally binding global climate agreement to put the world on track to avoid climate change by limiting global warming to well below 2°C. To achieve this, a 230 GW offshore wind capacity target for 2045 is estimated for the North Seas countries. As the renewable energy from the offshore industry is growing fast, the industry is facing new challenges. Wind farms are pushed towards more harsh environments, such as high current areas among others. In addition to wind energy, tidal energy from tidal turbine farms is under development. Prior to commissioning, installation of the turbines and the subsea power cables has to be made. Installation of power cables in high current seas can be very challenging. In order to maintain the structural integrity of the power cables and of the installation equipment, the dynamic behavior of the subsea cables has to be assessed.

During installation in high ocean currents, Vortex-Induced Vibrations (VIV) can occur. VIV is a result of vortices shedding behind the structure. These vortices can introduce vibrations that are perpendicular (crossflow) and parallel (in-line) to the flow direction. As a result, significant forces may arise, which can result in damage of the cable or compromising the installation procedure.

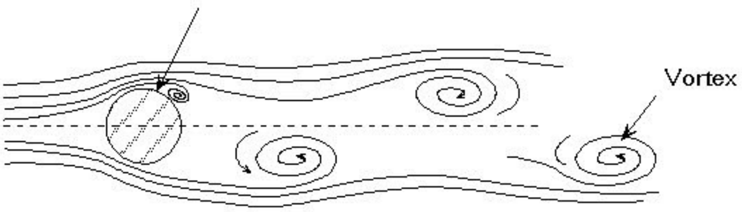

Figure 1.1: Vortex shedding behind a cable

Although a lot of research has been done regarding VIV on straight cylinders, not much work has been contacted on catenary shaped cables. Therefore, the aim of this thesis is to give an insight on the effects of VIV on the cables.

1.2. Research Objective

“To determine the influence of the VIV during subsea cable installation, ensure the cable integrity limits and provide solutions to improve workability”

1.3. Research Methodology

In order to tackle the above-mentioned challenge a research methodology was established and followed:

i. Literature Study

Background information is needed in order to gain a deep understanding on the phenomenon thus it can successfully analyzed lated on. Information on influencing parameters and previous work conducted is required to advance our research.

ii. Modeling

From the knowledge gained during the literature study, a suitable model to investigate the problem should be selected. At this stage a model needs to be created in a software, a programming language, etc., thus a tool will become available to analyze the problem.

iii. Model Validation

Before using the model in a case study, the model needs to be tested against experimental data or against other models and thus its validity can be assessed. Only after having successfully validated the model one can proceed in the next step.

iv. Case study

Finally a case study will be analyzed and numerous conclusions will be drawn.

1.4. Thesis outline

The current thesis report comprises of 6 chapters and is organized as follows:

Chapter 1, briefly gives a research background together with thesis problem description, objective and thesis outline.

Chapter 2, contains theory about VIV on straight,inclined and curved cylinders and the governing parameters which are involved.

Chapter 3, introduces the wake-structure model, which is based on the phenomenological model of the wake oscillator.

Chapter 4, includes the validation of the model against experimental data. Also, a a comparison between the wake-structure model and the Milan wake oscillator model from OrcaFlex’s VIV toolbox is presented.

Chapter 5, presents the VIV analysis of a case study.

Chapter 6, summarizes the conclusions of this thesis and provides recommendations for further research.

2

LITERATURE STUDY

2.1. Introduction

Vortex induced vibration (VIV) is a phenomenon that cylindrical structure may experience due to interactions between the structure and the flow. In this chapter, theory about the VIV and the important parameters which control it are described.

2.1.1. Fluid flow past cylinder

When fluid flows past a cylinder or other bluff body, it will be forced to change its original flowing path and move around the cylinder resulting in separated flow in the wake of the cylinder. Due to two layers of fluids moving in different velocities, vortices are formed. The different types of flow that can exist due to the flow separation are characterized by the Reynolds number, which is defined as following:

$$Re = \frac{V\ D}{v} \tag{2.1}$$

In which: V is the flow velocity $[m/s]$
D is the cylinder's diameter $[m]$
v is the kinematic viscosity of the fluid $[m^2/s]$

The different regimes of flow around a cylinder in a steady current can be seen in Figure 2.1. For Re values smaller than 40 there is no separation of the flow. In the range of $40 < Re < 150$ the first vortices are created and the vortex street remains laminar. In the range of $300 < Re < 3 * 10^5$ the vortex street is fully turbulent and it is known as the sub-critical flow regime.

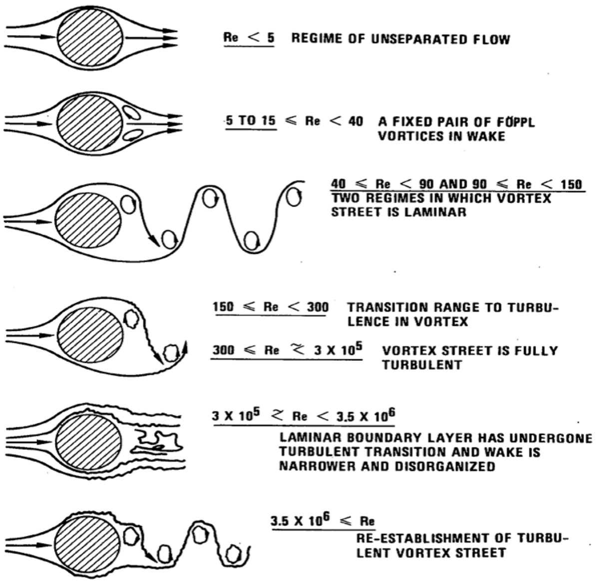

Figure 2.1: Regimes of flow around a smooth cylinder in steady current [Lienhard, 1966]

The vortices shed alternatively from both sides of the cylinder at a certain frequency. This frequency is known as the shedding frequency [Hz] and is defined as:

$$f_s = \frac{St\ V}{D} \tag{2.2}$$

In which: St is the Strouhal number [-]

The Strouhal number is an empirically derived value and it is depended on the Reynolds number. Their relation can be seen in Figure 2.2. In the sub-critical flow regime the Strouhal number is almost constant and equal with 0.2. For Re numbers higher than $3 * 10^5$ the St is increasing a bit for cylinders with rough surface and it is increases radically for cylinders with smooth surface.

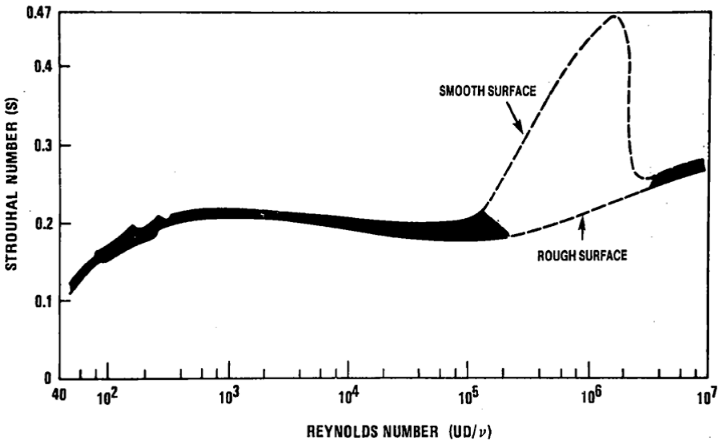

Figure 2.2: Relation between Strouhal number and Reynolds number [Lienhard, 1966]

2.2. Vortex forces on a cylinder

When the vortices shed alternately behind a cylinder, pressure variation occurs in the wake which results in an oscillating force. This force can be decomposed in two components; the in-line force, F_x which is the force in the flow direction and the cross flow force, F_y which is the force perpendicular to the flow direction . These forces differ in the case of a fixed-stationary cylinder and in the case of a free to move cylinder and will be discussed in the following section.

2.2.1. Stationary cylinder

In the case of a stationary rigid cylinder, the in-line force F_x is approximately the same with the drag force F_{Do} and the cross flow force F_y is approximately the same with the lift force F_{Lo}. An illustration of the forces resulting from the pressure variation can be seen in Figure 2.3 expressed in terms of force coefficients. Additional to the force resulting from the pressure variation, there are also viscous forces due to the friction on the surface of the cylinder but their contribution is small compared to the pressure forces and it is neglected. The lift force oscillates at the vortex shedding frequency f_s, while the drag force oscillates at twice the vortex shedding frequency.

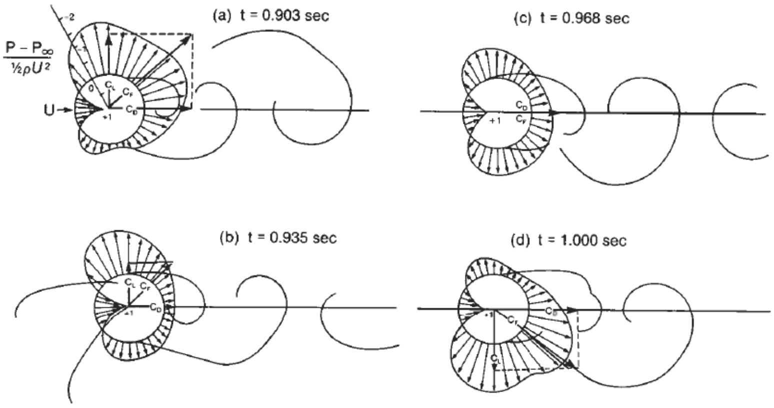

Figure 2.3: Pressure fields and wake forms [Drescher, 1956]

The drag and lift force can be expressed as a relation of non-dimensional coefficients in the form of Equation 2.3, respectively.

$$
\begin{aligned}
F_{Do} &= \frac{1}{2}\,\rho_w\ D\ L\ C_{Do}\ V^2 \\
F_{Lo} &= \frac{1}{2}\,\rho_w\ D\ L\ C_{Lo}\ V^2
\end{aligned}
\tag{2.3}
$$

In which:	C_{Do}	is the drag coefficient for a stationary cylinder [-]
	C_{Lo}	is the lift coefficient for a stationary cylinder [-]
	ρ_w	is the fluid density $[kg/m^3]$
	D	is the diameter of the cylinder $[m]$
	L	is the length of the cylinder $[m]$

In the following graphs the relation between the drag and lift coefficients and the Reynolds number is illustrated.

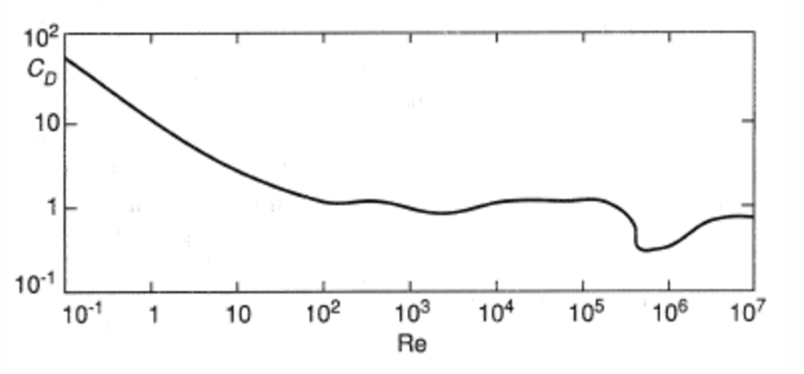

Figure 2.4: Mean drag coefficient against Reynolds number

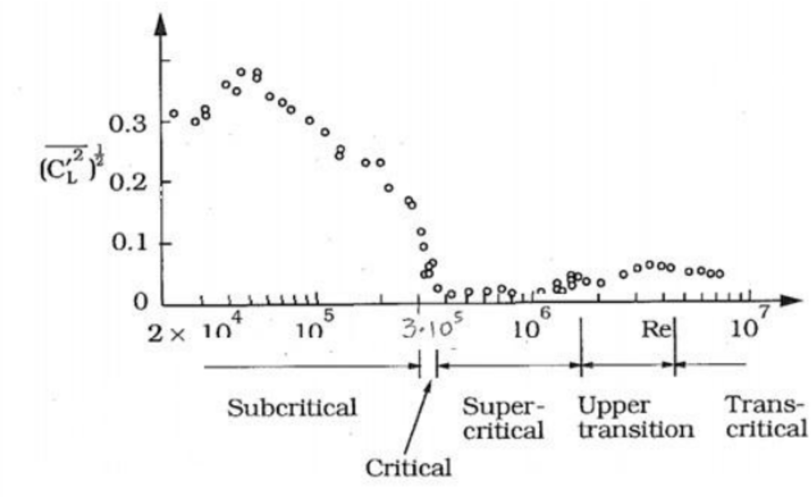

Figure 2.5: R.M.S of lift coefficient against Reynolds number

In the sub-critical region ($300 < Re < 3 * 10^5$) which is the regime of interest in this study, the mean value for the drag coefficient for a stationary cylinder is about 1.2. In the same regime the R.M.S of the lift coefficient lies between 0 and 0.4.

2.2.2. Moving cylinder

When the motion of the cylinder is significant, it affects the dynamics of the wakes, resulting in different drag and lift forces than for a stationary cylinder.

Drag force

For an oscillating cylinder a significant increase in the mean drag force is noticed, which can be related to the vibration amplitude. [Blevins, 1990] has proposed the following relation in order to account for drag amplification due to VIV for rigid cylinders:

$$C_d = C_{Do}\left[1 + 2.1\frac{A_y}{D}\right] \tag{2.4}$$

Where A_y is the maximum amplitude of the cross flow vibration.

For flexible risers the relationship proposed by [Vandiner J.K, 1983] is in good correspondence with experimental data:

$$C_d = C_{Do}\left[1 + 1.043\left(\frac{2A_{rms}}{D}\right)^{0.65}\right] \tag{2.5}$$

where A_{rms} is the root mean square of VIV amplitude.

The maximum amplitude of crossflow vibrations can be up to $1.2D$ which results in 3.5 times amplified drag coefficient in compasion with the one for a stationary cylinder. In Figure 2.6 the drag amplification due to VIV is plotted against the reduced velocity. The reduced velocity is a widely used parameter which can be defined as:

$$V_r = \frac{V}{f_n\ D} \tag{2.6}$$

Where f_n is the n^{th} natural frequency of the cylinder.

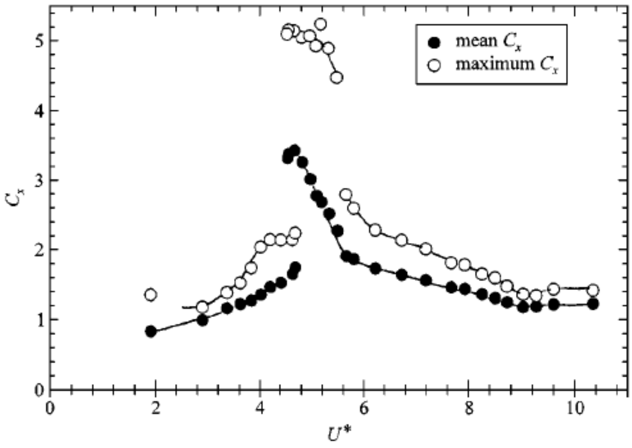

Figure 2.6: Drag amplification due to VIV [Khalak and Williamson, 1999]

Lift force

The lift force can be decomposed into a component in phase with the cylinder acceleration and a component in phase with the cylinder velocity. The lift force in phase with the acceleration provides an effective added mass for the system and the one in phase with velocity provides an effective damping. The latter determines if energy is transferred by the flow to the structure (if positive) or the other around if negative. This determines if the amplitude of oscillations increases or decreases and thus governs the self-limiting behavior of VIV. In Figure 2.7 the rms of the lift coefficient is plotted versus the reduced velocity.

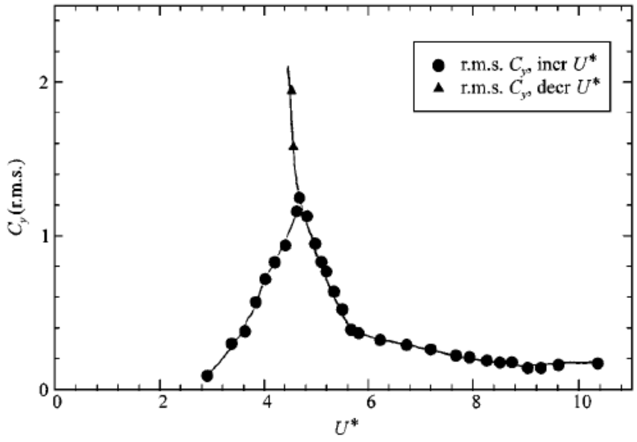

Figure 2.7: Lift variation due to VIV [Khalak and Williamson, 1999]

2.3. Vibration amplitude for a vertical cylinder

According to [Blevins and Coughran, 2009] three regimes of reduced velocities can be identified to assess the amplitude of the VIV. In Figure 2.8 the relationship between the in-line and cross flow vibration amplitude and the reduced velocity is illustrated. The three regimes can be defined as following:

- For $V_r < 3$ the vibration amplitude is small, the Strouhal equation is valid. The maximum vibration amplitude is about $0.1D$ and is a result of in-line VIV.
- For $4 < V_r < 11$ lock-in occurs, the vibration amplitude is maximized and the Strouhal equation is not valid anymore. The maximum vibration amplitude is about $1.2D$ at a reduced velocity of 7 and is a result of cross flow VIV. Lock-in is a complex phenomenon and is explained in more detail in Section 2.3.2.
- For $V_r > 11$ the shedding frequency unlocks from the natural frequency and the Strouhal equation becomes valid again. At these values of reduced velocities VIV is not present anymore.

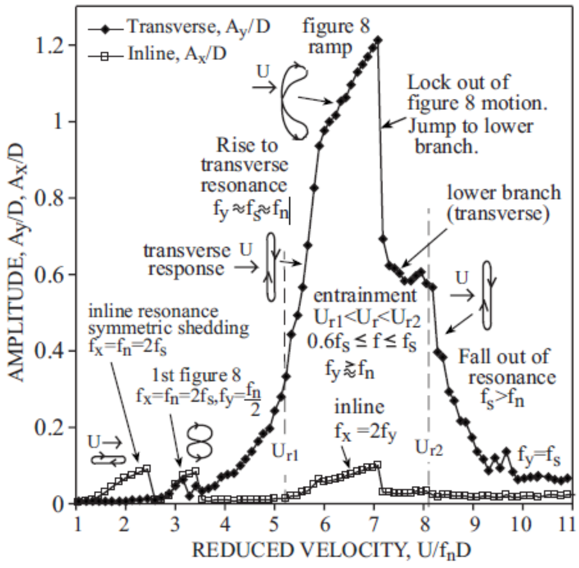

Figure 2.8: Vibration amplitudes as a function of reduced velocity [Blevins et al, 2009]

2.3.1. VIV response branches

There are three distinct VIV response branches as have been established by [Khalak and Williamson, 1999] in 1 DOF free vibration experiments for low mass-damping cylinders (cylinder is allowed to move only in the cross-flow direction). Namely, the initial branch, the lower branch and the upper branch. These branches have been also confirmed by [Jauvtis and Williamson, 2003] in 2 DOF free vibration experiments (cylinder is allowed to move both in the in-line and cross-flow direction). In Figure 2.9 one can observe the distinct branches. Black dots (•) represent the results when the cylinder is allowed to vibrate only in the cross flow direction and white dots (◦) represent the results when the cylinder is allowed to move in both the in-line and cross flow direction.

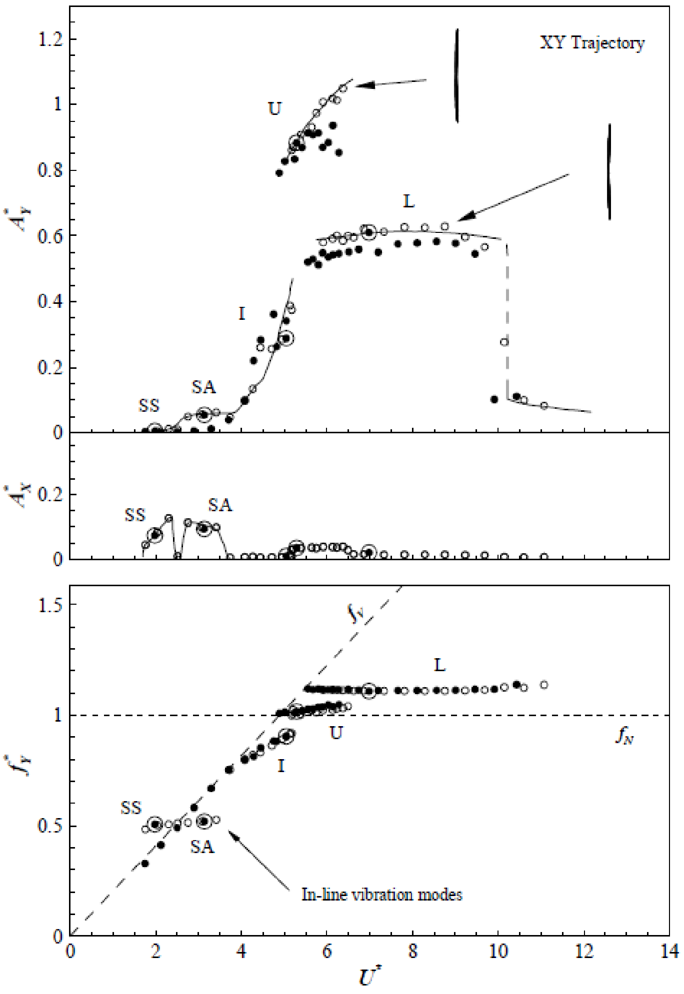

Figure 2.9: Distinct branches for low mass damping systems [Jauvtis and Williamson, 2003]

2.3.2. Lock-in

When the vortex shedding frequency is close to one of the natural frequencies of a structure, lock in or else synchronization can occur and the vibration amplitude is maximized. As the shedding frequency approaches the natural frequency of the structure, the Strouhal Equation 2.2 is not valid anymore and the shedding frequency becomes almost equal with the natural frequency. The reason that the shedding frequency is not exactly the same with the natural frequency is because of the interaction of the structure with the vortex shedding which consequently affects the added mass. Fluctuations in the added mass values result in fluctuations of the natural frequencies values.

If the lock-in happened when the natural frequency is exactly equal with the Strouhal frequency then:

$$V_r = \frac{V}{f_n\ D} = \frac{V}{f_s\ D} = \frac{V}{D}\frac{D}{S_t D} = \frac{1}{St} = 5 \tag{2.7}$$

However, lock-in usually occurs for the range of reduced velocities; $4 < V_r < 11$. Although this boundary is not fixed and depends on the mass ratio of the structure, as will be explained in Section 2.3.3.

2.3.3. Mass Ratio

One of the parameters that influence the amplitude and the lock in range of the VIV is the mass ratio. It can be defined as the mass m divide by the added mass m_a.

$$m^* = \frac{m}{m_\alpha} = \frac{m}{C_a \frac{\pi}{4} D^2 \rho_w} \tag{2.8}$$

Where, C_a is the potential added mass coefficient, equal to 1 in still water. When the cylinder oscillates, it forces the fluid particles to accelerate resulting in a force acting on the cylinder. This force is represented by the added mass. The C_a is a function of time, the shape of the body and its surroundings, the type of motion and orientation of the body through the fluid [Sarpkaya, 2003]. In Figure 2.10 from [Blevins and Coughran, 2009] the vibration amplitude and lock-in range dependence on the mass ratio can be seen.

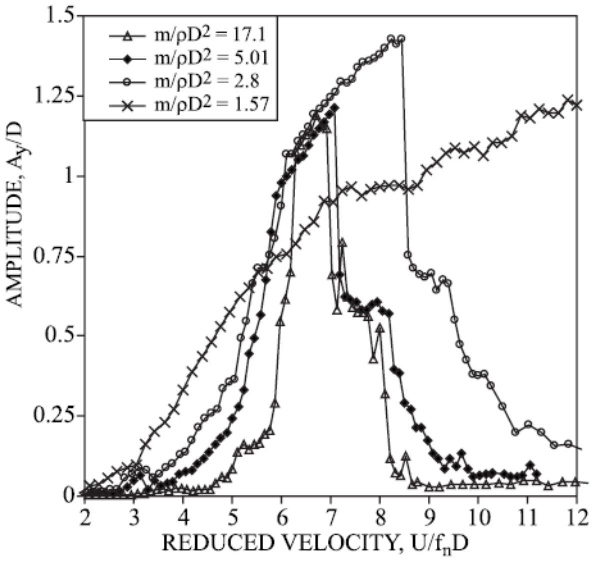

Figure 2.10: Vibration amplitudes for different mass ratios

From the above graph it can be observed that as the mass ratio decreases, the vibration amplitude and lock-in range become larger. The explanation of the latter lies on the variation of the added mass coefficient with the reduced velocity. In Figure 2.11 one can observe that the added mass coefficient reduces monotonically with increasing reduced velocity. As a result, as the reduced velocity increases, the natural frequency of the cylinder is increasing as well. Therefore the ratio of the shedding frequency divided by the oscillation frequency remains closer to 1 (synchronization) over a broader range of flow speeds. For lower mass ratio the contribution of added mass on the natural frequency is bigger resulting in extended lock-in ranges.

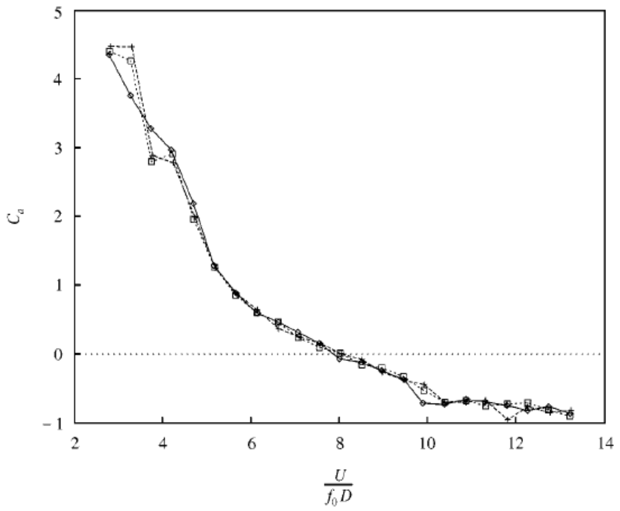

Figure 2.11: Added mass coefficient versus reduced velocity [Vikestad et al., 2000]

2.4. VIV on inclined cylinders

In the majority of studies on VIV the flow direction is perpendicular to the long axis of the structure. However, in the case of a subsea power cable and many other offshore engineering applications, the direction of the flow is not usually perpendicular to the structure.

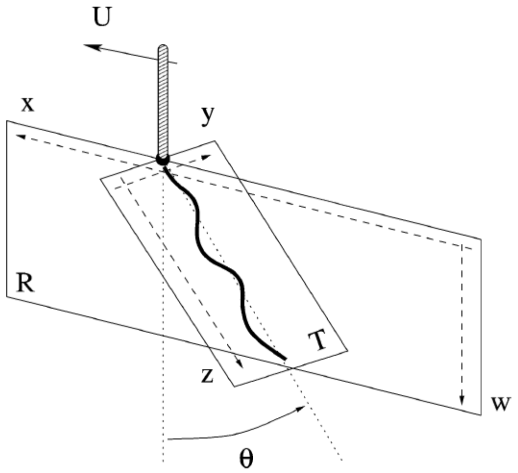

Figure 2.12: Inclined cable motion [Facchinetti et al., 2003]

[Jain and Modarres-Sadeghi, 2013] performed experiments on a flexibly mounted inclined rigid cylinder up to an angle of inclination of $\theta = 75°$ and Reynolds range of $Re = 500 - 4000$ to study the influence of inclination on the resulting vortex induced vibrations. From this research the following observations have been made:

- Angles of inclination up to 45° ($\theta < 45°$) do not result in any deduction in the maximum amplitude of oscillations. For angles $\theta > 45°$ the peak amplitude is decreased with increasing angle of inclination.
- As the angle of inclination is increased the lock-in range starts at higher reduced velocities or else the lock-in region delays.
- Negative angles of inclination result in increased width of the lock-in region. (A cylinder

inclined away from the oncoming flow is considered to have a positive angle of inclination)
• The vortex shedding is forced to be parallel to the movement of the cylinder (Figure 2.13).

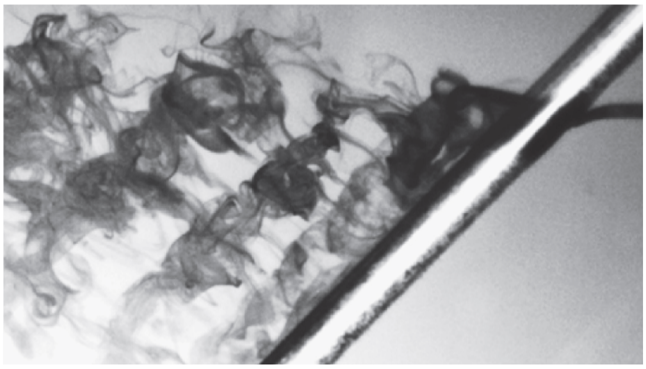

Figure 2.13: Flow visualization in the wake of a 45° inclined cylinder [Jain and Modarres-Sadeghi, 2013]

To assess the vortex shedding behind a cylinder the Independence Principle (IP) is widely used. The IP neglects the axial component of the flow and considers only the component of the velocity normal to the cylinder axis.

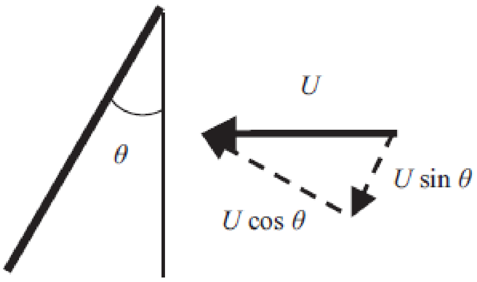

Figure 2.14: Inclined cylinder with the normal and axial components of the flow velocity [Jain and Modarres-Sadeghi, 2013]

In the case of an inclined cylinder the Strouhal frequency or shedding frequency reads as:

$$f_s = \frac{St\ V \cos\theta}{D} \tag{2.9}$$

As regards the validity of the IP it was observed that:

• The width of the lock-in region is the same for $\theta < 45°$, and decreases significantly for $\theta > 45°$.
• For $\theta > 45°$ the lock-in range changes its pattern and the relatively wide plateau of the large amplitude oscillations observed for the lower angles of inclination disappears, and instead, the large amplitude oscillation occurs over a very short range of normalized reduced velocities.

2.5. VIV on curved cylinders

[Assi et al., 2014] conducted 2D VIV experiments to investigate the response of a rigid curved circular cylinder with low mass-damping ratio ($m^* = 2.1, m^*\zeta = 0.0042$). The flow profile was uniform and Reynolds number ranged between 750 and 15000. Two curved configurations, a concave and a convex, were tested regarding the direction of the flow and the results were compared with a reference straight cylinder. Convex configuration is when the plane of curvature of the body is aligned to the flow direction such that the outer part of the ring is the body's stagnation face. Similarly, concave configuration is when the inner part of the ring is the body's stagnation face.

Figure 2.15: Flow visualization for a curved cylinder in uniform flow parallel to the plane of curvature $Re = 100$ [Miliou et al., 2003]

In this study among other, the following conclusions were made:

- A curved rigid cylinder presents lower peak of amplitude of vibration in both the crossflow and in-line direction when compared to a straight cylinder.

- Although the peak amplitude is reduced, a curved cylinder may present a significant level of vibration that is sustained for higher values of reduced velocity beyond the end of the typical synchronization range.

The above conclusions are presented graphically in Figures 2.16 and 2.17.

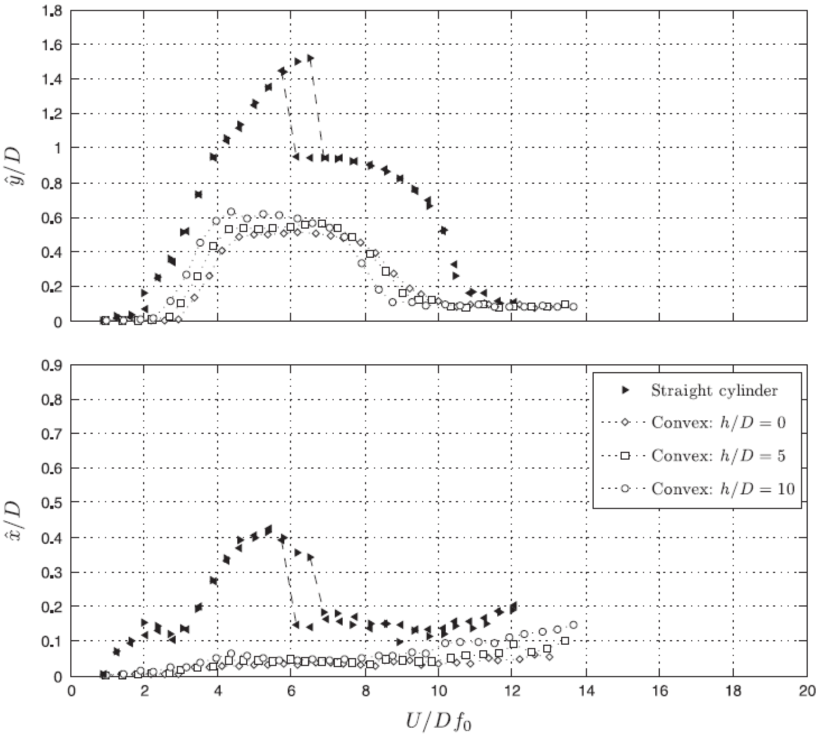

Figure 2.16: Crossflow and in-line amplitude of vibration versus reduced velocity for a straight cylinder and convex configurations varying the vertical section length [Assi et al., 2014]

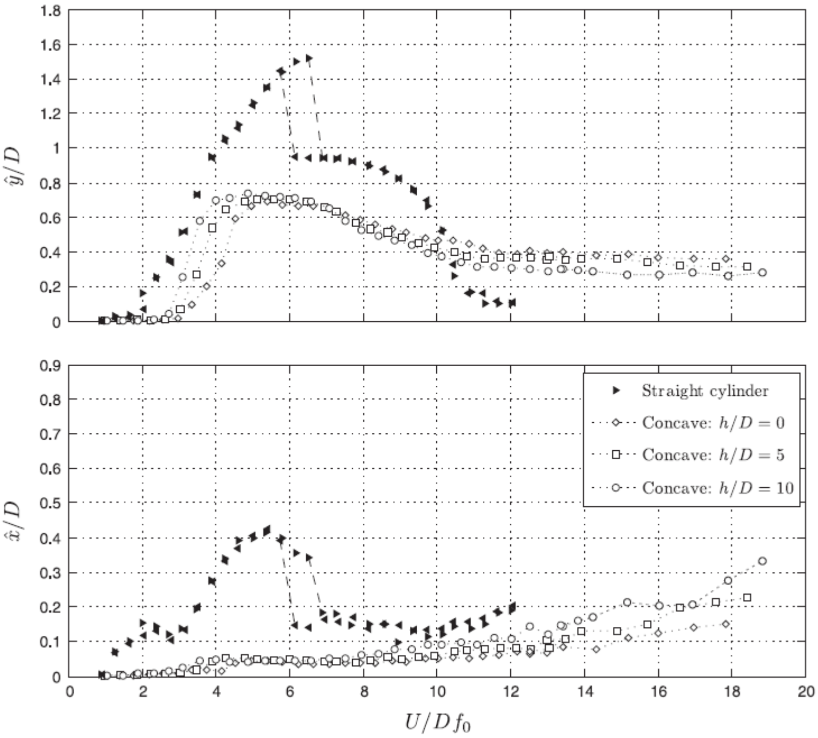

Figure 2.17: Crossflow and in-line amplitude of vibration versus reduced velocity for a straight cylinder and concave configurations varying the vertical section length [Assi et al., 2014]

2.6. Chapter summary

In this chapter the basic principles which govern the VIV have been presented. As illustrated VIV is a complex phenomenon which depends significantly on the structure properties, the flow characteristics and the interaction between them. Cross flow vibration amplitudes can be up to 10 times higher than the in-line ones. Also, there are significant differences between VIV on vertical and on inclined and curved cylinders. In the next chapter a model capable of predicting the VIV amplitude and frequency response is presented.

3

VIV MODEL

3.1. Wake oscillator

The fluctuating nature of the vortex street is modeled by a non-linear oscillator satisfying the Van der Pol equation. The latter can capture well, self-limiting, self-exciting phenomena which include a lock-in regime, such as the VIV. The modified Van der Pol model is given by the equation:

$$\ddot{q} + \epsilon\omega_s(q^2 - 1)\dot{q} + \omega_s^2 q = F(t) \tag{3.1}$$

Where:		
	q	is the wake variable [-]
	ϵ	is a tuning parameter [-]
	ω_s	is the natural frequency of the oscillator $[rad/s]$
	$F(t)$	is the forcing term

The dimensionless wake variable q is associated to the fluctuating lift coefficient C_L. The natural frequency of the oscillator is chosen to be the same with the vortex shedding frequency, as defined in Equation 2.2.

The self-limiting, self-exciting behavior of the VIV is controlled by the damping term: $\epsilon\omega_s(q^2 - 1)\dot{q}$. When $q^2 - 1 < 0$ the damping term is negative, there is energy input in the system and the q increases. When $q^2 - 1 > 0$ the damping term is positive then the q decreases. If the oscillator is unforced ($F(t) = 0$), then it provides a quasi-harmonic oscillation with amplitude $q = 2$ at the angular frequency ω_s. Appendix A gives examples on how a Van del Pol oscillator works.

The forcing term at the right-hand side models the effects of the cylinder motion on the near wake. Different coupling models have been proposed over the years, such as displacement, velocity and acceleration coupling. [Facchinetti et al., 2003] concluded that acceleration coupling can capture the features of VIV better than the rest. Applying the acceleration coupling, the equation reads as:

$$\ddot{q} + \epsilon\omega_s(q^2 - 1)\dot{q} + \omega_s^2 q = \frac{A}{D}\frac{d^2y}{dt^2} \tag{3.2}$$

Where:		
	A	is a tuning parameter [-]
	D	is the cylinder's diameter $[m]$
	$\frac{d^2y}{dt^2}$	is the cross-flow acceleration of the cylinder $[m/s^2]$

At the following section the influence of the tuning parameters A and ϵ on the behavior of the wake oscillator is explained.

3.2. Influence of the parameters A and ϵ

The behavior of the wake oscillator is determined by the values of the parameters A and ϵ. The vibration amplitude and the lock-in region depend highly on these values. Some remarks on how each of the tuning parameters influences the wake oscillator are presented herein:

Parameter ϵ:

- Larger ϵ results in reaching faster the steady state response.

Parameter ϵ is associated with the damping term $\epsilon\omega_s(q^2-1)\dot{q}$. For small initial value of q then the term is negative and there is energy input in the system (negative damping). The bigger the ϵ the higher the energy input in the system, thus the steady state response is reached faster.

- Larger ϵ results in smaller maximum steady state amplitude.

Again, because the parameter ϵ controls the damping term, when the steady state is reached there is higher damping in the system with large values of ϵ, which results in smaller maximum steady state amplitudes.

- Larger ϵ results in wider lock in range

In Figure 3.1 the above-mentioned influence of the tuning parameter ϵ can be seen graphically.

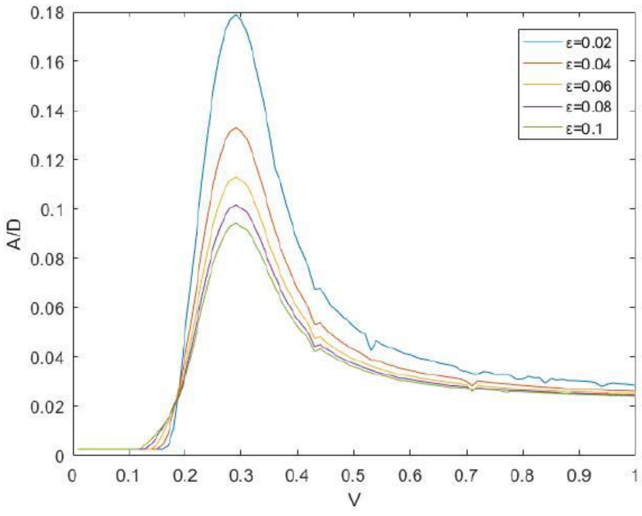

Figure 3.1: Effect of tuning parameter ϵ [Sun, 2017]

Parameter A:

- Larger A results in larger maximum steady state amplitude.

Parameter A is associated with the forcing term $\frac{A}{D}\frac{d^2y}{dt^2}$, thus the bigger the A the bigger the external force which finally gives larger amplitudes.

- Larger A results in wider lock in range

In Figure 3.2 the influence of the tuning parameter A can be seen graphically.

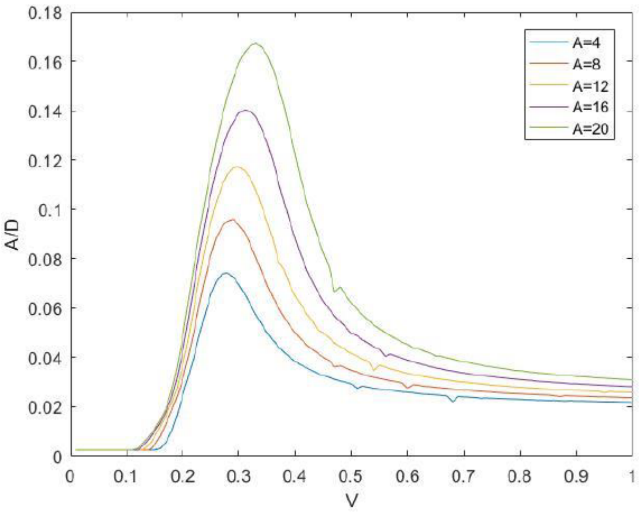

Figure 3.2: Effect of tuning parameter A [Sun, 2017]

3.3. Tuning of the parameters A and ϵ

To tune correctly the parameters, a comparison with experimental results has to be done and fitting of the parameters accordingly. [Ogink and Metrikine, 2010] have proposed 2 sets of parameters after tuning their model with the 1-DOF free vibration experiments of [Khalak and Williamson, 1999]. Specifically, they determined values for the upper branch “Case U” and for the lower branch “Case L”. They have concluded that tuning the wake oscillator with one set of frequency depended parameters for both branches is not yet possible.

[Slingsby, 2015] tuned the wake oscillator parameters against the 2-DOF experiment of [Blevins and Coughran, 2009]. Instead of two sets of parameters for the upper and lower branch he attempts to use one set only, which works approximately good for both. Also he determined different set of parameters for very low mass ratio systems ($m^* < 1.57$) and higher mass ratio systems ($m^* > 1.57$). The values used in both researches can be seen in Table 3.1.

Table 3.1: Values of A and ϵ according to previous researches

	[Ogink and Metrikine, 2010]		[Slingsby, 2015]	
Parameter	Upper Branch	Lower Branch	$m^* > 1.57$	$m^* < 1.57$
A	4.0	12.0	10.0	19.0
ϵ	0.05	0.7	0.07	0.3

The above values will be used further on, in this research. In Appendix G the model fitting to the experimental results in the above mentioned researches can be found.

3.4. Coupling of the wake oscillator and the structure

In this research the structural response is obtained by the finite element software OrcaFlex (ref. Appendix F). However, the simple case of a two degree of freedom (2DOF) elastically supported rigid circular cylinder will be used here to illustrate the coupling between the structure and the wake.

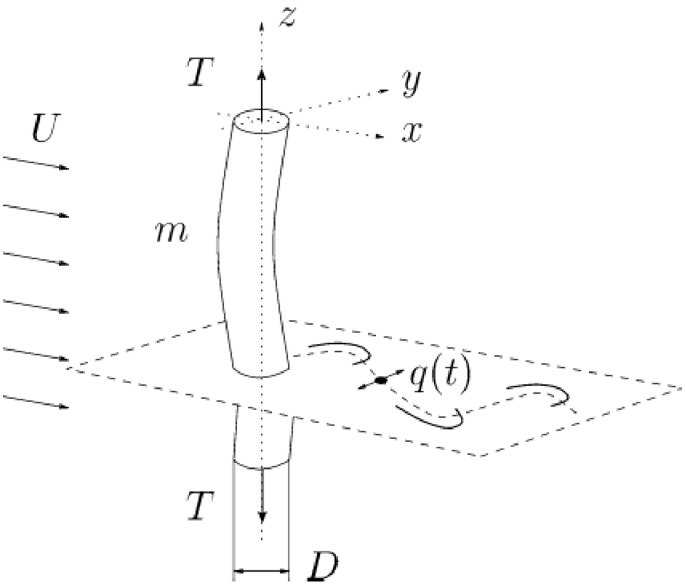

Figure 3.3: Fluid structure model: a very slender tensioned cable in stationary uniform flow. [Facchinetti et al., 2004]

The equation of motion for a rigid cylinder on viscoelastic supports read as:

$$\begin{aligned} (m + m_\alpha)\ddot{x} + c\dot{x} + kx &= F_x(t) \\ (m + m_\alpha)\ddot{y} + c\dot{y} + ky &= F_y(t) \end{aligned} \tag{3.3}$$

Where:

m	is the mass per unit length $[kg]$
m_α	is the added mass per unit length $[kg]$
c	is the damping coefficient $[kg/s]$
k	is the spring coefficient $[N/m]$

The forces acting on the in-line and crossflow direction can be expressed as a relation of non-dimensional coefficients in the form of Equation 3.4, respectively.

$$\begin{aligned} F_x &= \frac{1}{2}\,\rho_w\; D\; L\; C_{VX}\; V^2 \\ F_y &= \frac{1}{2}\,\rho_w\; D\; L\; C_{VY}\; V^2 \end{aligned} \tag{3.4}$$

3.5. Force Decomposition

The in-line force F_{VX} is the not the same with the drag force F_{VD} and the cross flow force F_{VY} is not the same with the lift force F_{VL} as can be seen in Figure 3.4 (in contrast with the case of a stationary cylinder). The drag force is always in line with the *relative* flow direction and the lift force is always perpendicular with the relative flow direction. Therefore a decomposition needs to be made in order to express the in-line and crossflow coefficients, C_{VX} and C_{VY}, into drag and lift coefficients, C_{VD} and C_{VL}.

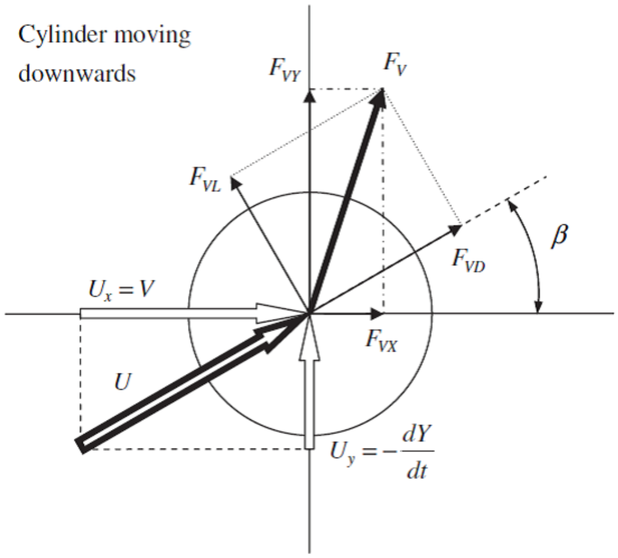

Figure 3.4: Decomposition of the vortex fluid drag force [Ogink and Metrikine, 2010]

Undisturbed flow velocity: $V_x = V\cos\alpha$, $V_y = V\sin\alpha$, $V = \sqrt{V_x^2 + V_y^2}$

Relative flow velocity: $U_x = V_x - \frac{dx}{dt}$, $U_y = V_y - \frac{dy}{dt}$

$U_x = U\cos\beta$, $U_y = U\sin\beta$, $U = \sqrt{U_x^2 + U_y^2}$

α is the angle between the undisturbed flow direction and the X axis
β is the angle between the relative flow direction and the X axis

Decomposing the forces acting on the cylinder in the X and Y direction reads as:

$$\begin{aligned} F_{VX} &= F_{VD}\cos\beta - F_{VL}\sin\beta \\ F_{VY} &= F_{VD}\sin\beta + F_{VL}\cos\beta \end{aligned} \tag{3.5}$$

Substituting the forces with their equivalent expressions results in:

$$\begin{aligned} \frac{1}{2}\rho_w D L C_{VX} V^2 &= \frac{1}{2}\rho_w D L C_{VD} U^2 \cos\beta - \frac{1}{2}\rho_w D L C_{VL} U^2 \sin\beta \\ \frac{1}{2}\rho_w D L C_{VY} V^2 &= \frac{1}{2}\rho_w D L C_{VD} U^2 \sin\beta + \frac{1}{2}\rho_w D L C_{VL} U^2 \cos\beta \end{aligned} \tag{3.6}$$

Rearranging the equations for the force coefficients in the X and Y direction results in:

$$\begin{aligned} C_{VX} &= (C_{VD}\cos\beta - C_{VL}\sin\beta)\frac{U^2}{V^2} = (C_{VD}U_x - C_{VL}U_y)\frac{U}{V^2} \\ C_{VY} &= (C_{VD}\sin\beta + C_{VL}\cos\beta)\frac{U^2}{V^2} = (C_{VD}U_y + C_{VL}U_x)\frac{U}{V^2} \end{aligned} \tag{3.7}$$

Substituting the above expressions in the force formula gives:

$$\begin{aligned} F_x &= \frac{1}{2}\rho_w DL(C_{VD}U_x - C_{VL}U_y)U \\ F_y &= \frac{1}{2}\rho_w DL(C_{VD}U_y + C_{VL}U_x)U \end{aligned} \tag{3.8}$$

At this point, the wake forces acting in the X and Y direction have been formulated in terms of drag and lift coefficients that are known from experiments instead of lateral and vertical coefficients that are unknown. The next step is to couple these forces with the wake variable q.

According to [Facchinetti et al., 2003] the drag component of the vortex force is constant and the lift component is linearly related to the wake variable q. The drag coefficient is chosen the same with the one for a stationary cylinder $C_{VD} = C_{Do}$ and the lift coefficient is equal with:

$$C_{VL} = \frac{C_{Lo}}{2}q \tag{3.9}$$

The values for the stationary coefficients can be derived experimentally and have been discussed in section 2.2.1.

Substituting equation 3.9 in 3.8, the final expression for the wake force has been derived:

$$\begin{aligned} F_x &= \frac{1}{2}\rho_w DL(C_{Do}U_x - \frac{C_{Lo}}{2}qU_y)U = \frac{1}{2}\rho_w DLC_{Do}U_xU - \frac{1}{2}\rho_w DL\frac{C_{Lo}}{2}qU_yU \\ F_y &= \frac{1}{2}\rho_w DL(C_{Do}U_y + \frac{C_{Lo}}{2}qU_x)U = \frac{1}{2}\rho_w DLC_{Do}U_yU + \frac{1}{2}\rho_w DL\frac{C_{Lo}}{2}qU_xU \end{aligned} \tag{3.10}$$

3.6. Modeling of the wake-structure interaction

In the previous section the coupled wake-structure model was introduced. In this section the realization of the model is briefly discussed. In Figure 3.5 it is visualized how the coupling between OrcaFlex (structure) and the external function in Python (wakes) works.

At every time step OrcaFlex gives as an input in the external function the relative velocity in the X and Y direction (U_x, U_y) and the cross-flow acceleration (α_y) for a node. Then inside the function using an ODE solver, namely “dopri5” based on Runge-Kutta 4 (ref. Appendix E), the wake variable q is calculated and further the wake forces in the in-line and crossflow direction (F_x, F_y) are calculated. Next, python gives as an input in OrcaFlex the latter forces and the new position of the node is calculated. This process is repeated for every node of the line for the current time step and then the whole process is repeated for every time step.

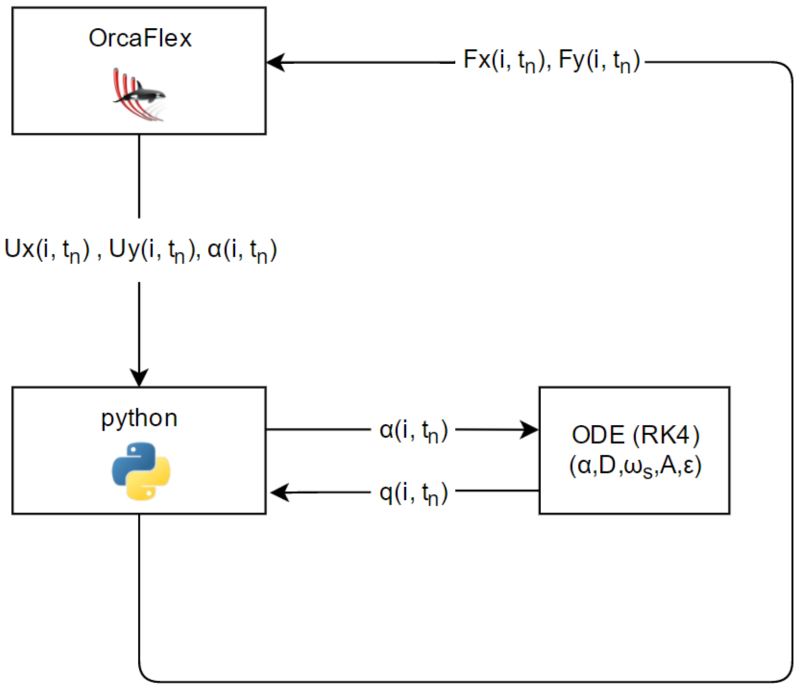

Figure 3.5: Coupling between OrcaFlex and the external function in python

$U_x(i, t_n)$	is the relative velocity in the X direction of the node i at the timestep t_n
$U_y(i, t_n)$	is the relative velocity in the Y direction
$\alpha_y(i, t_n)$	is the acceleration in the Y direction
$q(i, t_n)$	is the wake variable
$F_x(i, t_n)$	is the force generated by the wake in the in-line direction
$F_y(i, t_n)$	is the force generated by the wake in the crossflow direction
i	is the node for which the external function is called, $i = 1, ..., n$ where n is the total number of nodes
t_n	is the current timestep, $t_n = 0, ..., t_{max}$

3.7. Chapter summary

In this chapter a wake oscillator model capable of representing the VIV phenomenon was introduced. This phenomenological model is based on the Van der Pol equation and it is coupled with the structure through the structure's acceleration. The tuning parameters controlling the model have been discussed and suitable values have been chosen. Also, the modeling of this couple wake-oscillator model has been briefly presented. In the next chapter, model validation is done by comparison with experimental results and OrcaFlex's VIV models.

4

MODEL VALIDATION

After creating the coupled structure-wake oscillator model, it is important to validate it against real data. For this purpose, the model is tested against the results of two experiments. First, the case of a vertical riser is examined (Delft Flume experiment), and secondly the more complex case of a catenary riser is examined (Instituto de Pesquisas Technologicas of São Paulo). Also the model is compared with Milan wake oscillator model of OrcaFlex's VIV toolbox.

4.1. Delft Flume experiment

A series of tests were carried out on a riser model in the flume of Delft Hydraulics laboratory by [Chaplin et al., 2005b]. Different measurements of the vortex induced vibrations on the vertical tension riser in a stepped current were conducted. The upper part of the riser (55% of the total length) was in still water, while the lower part of the riser (45%) was exposed to a uniform current at speeds up to $1m/s$. The carriage was moving along the flume to generate steady current conditions. The experimental arrangement is shown in Figure 4.1.

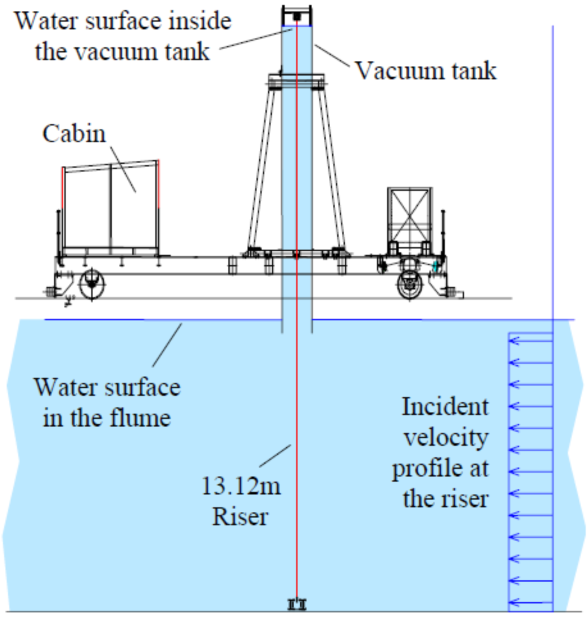

Figure 4.1: Layout of Delft Flume experiment

At the following table the riser details and properties are presented.

Table 4.1: Riser parameters

Diameter	$D = 0.028\ m$	Bending Stiffness	$EI = 29.9\ Nm^2$
Riser length	$L = 13.12\ m$	Axial Stiffness	$EA = 5.88\ MN$
Mass ratio	$m^* = 3$	Structural damping	$\zeta = 0.0033$
Total weight	$W = 18.13\ N/m$	Weight in water	$W_s = 12.1\ N/m$
Water density	$\rho_w = 1000\ kg/m^3$	Kinematic viscosity	$\nu = 1.12 * 10^{-6}\ m^2/s$

4.1.1. Model Description

In the experiment the riser was installed with universal joints at each end and at the top it was suspended by a tensioning system. To reproduce accurately the boundary conditions of the structure in the OrcaFlex model, the top node is suspended by an OrcaFlex winch and the bottom node of the line is hinged (translational DOF are constrained and rotational are free). The top node can move axially but the lateral displacement is constrained. Uniform steady current is applied to the lower 45% of the line. The length of each element was selected to be $0.2m$. In Figure 4.2 the OrcaFlex model is illustrated and one can see the applied boundary conditions.

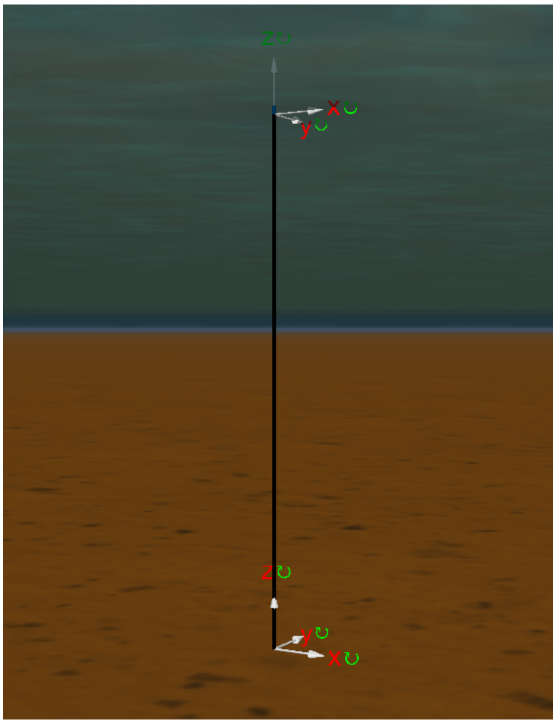

Figure 4.2: Delft experiment-Orcaflex model artistic view

As regards the wake oscillator model parameters, three different sets of tuning parameters were examined and for all the tests the drag coefficient, the lift coefficient and the Strouhal number were kept the same.

Table 4.2: Wake model parameters

A	10	4	12
ϵ	0.07	0.05	0.7
C_d	1.1856	1.1856	1.1856
C_l	0.3842	0.3842	0.3842
St	0.1938	0.1938	0.1938

In the experiment different cases were examined, with different towing speeds and top tensions. In this study, three different cases were selected and their values are summarized in Table 4.3.

Table 4.3: Loadcases Delft experiment

Case	Towing speed (m/s)	Top tension (N)	Re
3	0.31	457	7800
6	0.60	670	15000
9	0.95	1002	24000

4.1.2. Natural Frequencies

From the experiment the first 7 eigenfrequencies are available for comparison. The natural frequencies were measured in still water top tension of 813 N. In Table 4.4 below, the values of eigenfrequencies measured from the experiment and the ones calculated in OrcaFlex are presented.

Table 4.4: First 10 Natural Frequencies of the riser

Mode number	OrcaFlex (Hz)	Experimental (Hz)
1	0.655	0.633
2	1.314	1.329
3	1.982	1.954
4	2.662	2.625
5	3.359	3.312
6	4.075	4.028
7	4.814	4.753
8	5.579	-
9	6.372	-
10	7.196	-

The calculated eigenfrequencies by OrcaFlex are in a good agreement with the measured experimental ones; the difference is about 1.5%.

4.1.3. Results

In Figure 4.3a the envelope of the crossflow displacement along the riser's length is illustrated for three different sets of tuning parameters. From the shape of the graph it is evident that the riser is vibrating at the 4^{th} mode shape. This can be confirmed also from the Figure B.1a in which the spectral density of the crossflow displacement and the natural frequencies of the riser have been plotted together. In Figure 4.3b the envelope of the in-line displacement along the riser's length is presented.

- $\boldsymbol{Case\ 3 - V = 0.31m/s\ and\ T_{top} = 457N}$

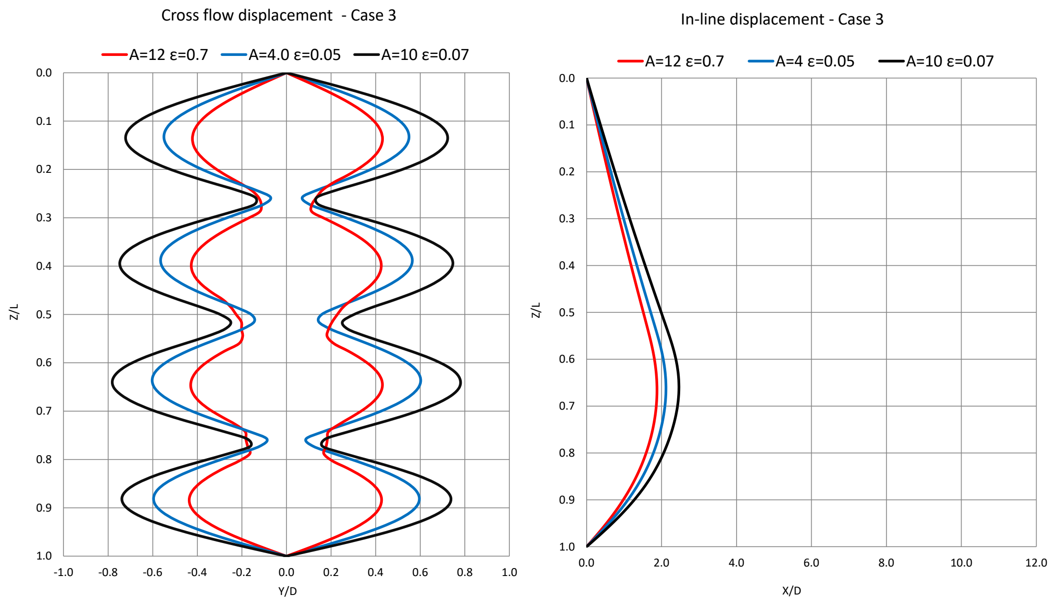

(a) (b)

Figure 4.3: Case 3-Envelope (a) crossflow (b) in-line displacement

Similar as in Case 3, in Case 6 the vibration mode of the riser is evident, and it vibrates with frequency near to its 6^{th} natural frequency, thus the 6^{th} mode shape can be seen in Figure 4.4a.

- $\boldsymbol{Case\ 6 - V = 0.60m/s\ and\ T_{top} = 670N}$

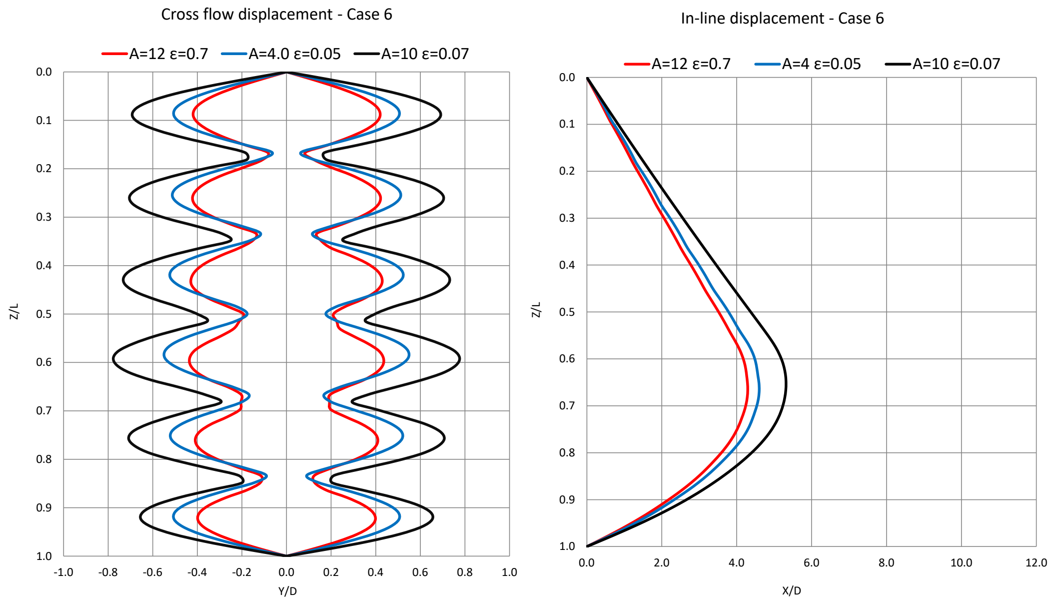

(a) (b)

Figure 4.4: Case 6-Envelope (a) crossflow (b) in-line displacement

- ***Case* $9 - V = 0.95m/s$ *and* $T_{top} = 1002N$**

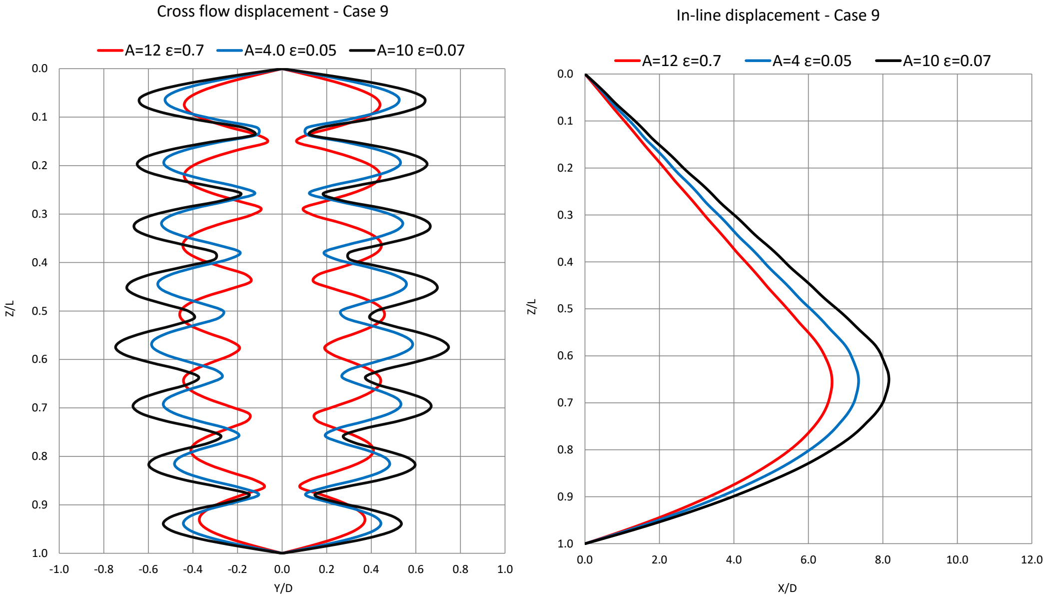

(a) (b)

Figure 4.5: Case 9-Envelope (a) crossflow (b) in-line displacement

In Figure 4.6, the experimental results as presented in [Chaplin et al., 2005a] are illustrated.

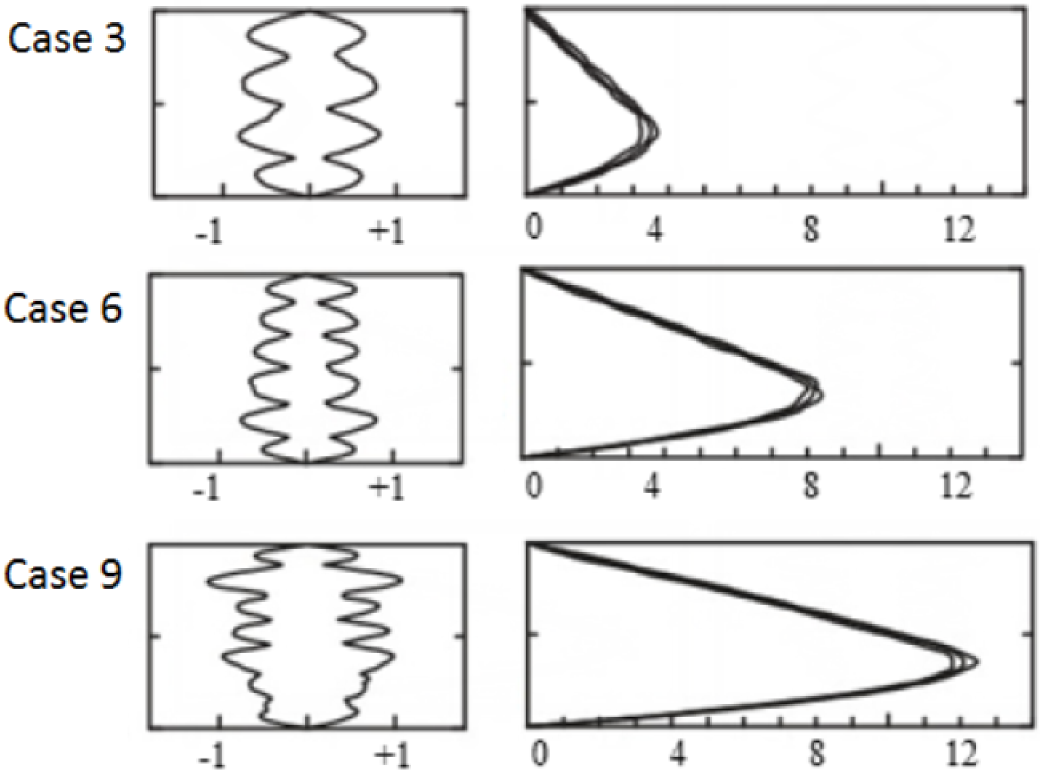

Figure 4.6: Experimental measurements

Comparing the results of the numerical model against the experimental measurements (Figure 4.6), the following observations can be made:

- The model captures well the dominant vibration mode.

- The set of tuning parameters $A = 10$, $\epsilon = 0.07$ achieves crossflow vibration amplitudes closer to the experimental ones and also predicts better the mean in-line displacement, thus this set is going to be used further in this thesis.

- The mean in-line displacement is underestimated about 30-50% depending on the set of tuning parameters. This can be attributed partly to the presence of springs at the top of the riser which added considerably to the complexity of computing large amplitude displacements, as also pointed out by [Chaplin et al., 2005a]. Therefore the underestimation of the in-line displacement is associated with (a) the modeling of the boundary conditions (top springs) of the experiment and (b) the wake oscillator model itself. It is known from Ogink and Metrikine [2010] that the wake oscillator model underestimates the mean in-line force for a certain range of reduced velocities and amplitudes, but this specific experiment is not suitable (due to the presence of the springs) for deriving any conclusions regarding the underestimation of in-line displacement by the wake oscillator model.

- The results of the in-line displacement presented herein are closer to the experimental than the results in the research of [Slingsby, 2015] because although the set of tuning parameters is the same, the end nodes were considered fixed in his study.

In Appendix B further results can be found regarding spectral frequencies and timehistory results for the different set of tuning parameters. In addition OrcaFlex's VIV models were used and the results are compared with the Orcina's published reports.

4.2. São Paulo experiment

A model test with a steel catenary riser (SCR) was conducted in the towing tank at the Instituto de Pesquisas Technologicas of São Paulo by [Morooka and Tsukada, 2013]. The main goal of these experiments was to determine the global response of a SCR model to VIV forces. The top of the riser was attached to a load cell which measures the riser top tension and the bottom of the riser was supported by a metallic bottom floor. The end of the riser was attached to a plastic sleeve fixed at the bottom floor. Uniform current conditions were generated by moving the carriage at almost constant speed. The test setup is illustrated in Figure 4.7.

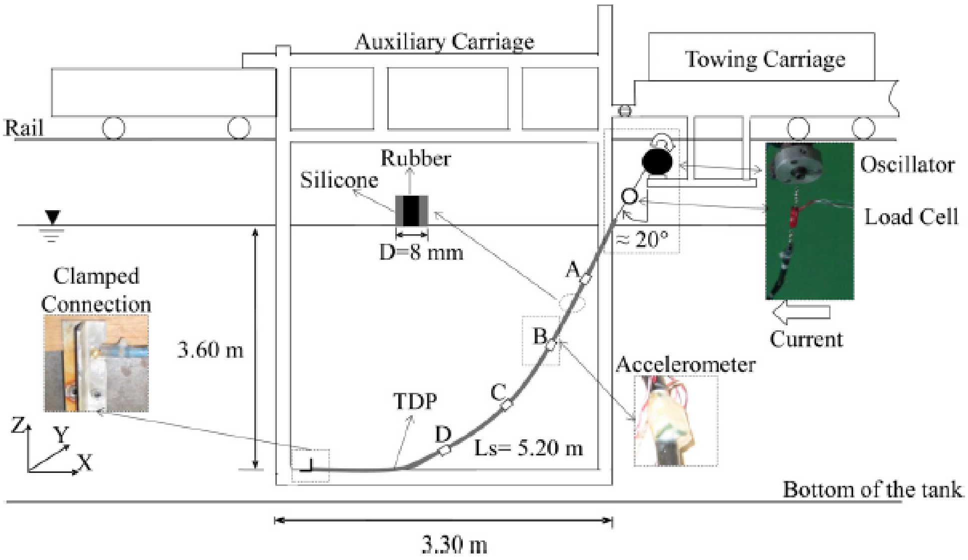

Figure 4.7: Layout of São Paulo experiment

Table 4.5 presents the properties for the actual experimental model.

Table 4.5: Actual experimental model SCR parameters

Total length	$L = 7.52\ m$	Suspended length	$L_s = 5.2\ m$
Depth	$H = 3.6\ m$	Inclination top angle	$\theta = 20°$
Axial Stiffness	$EA = 13.75\ N$	Bending Stiffness	$EI = 5.5 * 10^{-5}\ Nm^2$
Diameter	$D = 8.0 * 10^{-3}\ m$	Mass ratio	$m^* = 1.25$
Water density	$\rho_w = 1000\ kg/m^3$	Kinematic viscosity	$\nu = 1 * 10^{-6}\ m^2/s$

4.2.1. Model description

To represent the boundary conditions of the experiment the top node has been considered pinned and the bottom node of the line has been considered clamped. The length of each element was selected to be $0.1m$. Uniform steady current is applied to the whole line and the current flow direction is aligned with the plane of curvature of the catenary riser. The outer part of the catenary is the stagnation face of the structure. In Figure 4.8 an artistic impression of the OrcaFlex model can be seen.

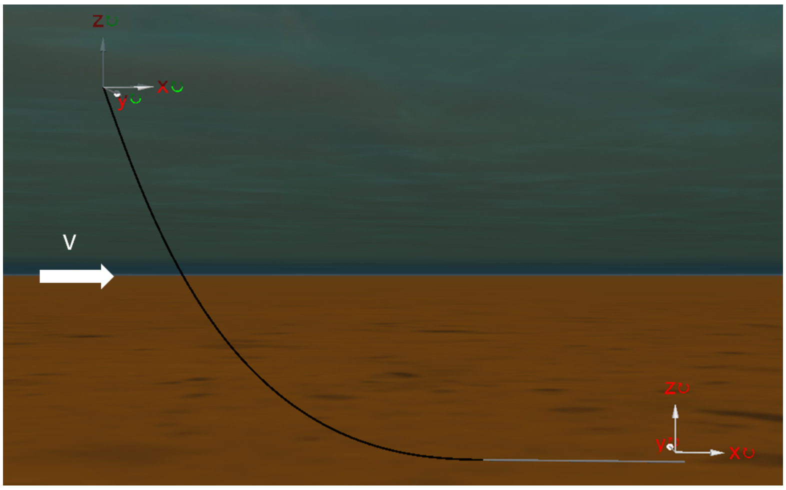

Figure 4.8: São Paulo OrcaFlex model artistic view

In Table 4.6 the loadcases are summarized.

Table 4.6: Loadcases São Paulo experiment

Case	Towing speed (m/s)	Top tension (N)	*Re*
I	0.00	385	0
II	0.05	353	400
III	0.07	317	560

For the wake oscillator model the following parameters were selected: $A = 10$, $\epsilon = 0.07$, $C_d = 1.2$, $C_l = 0.4$ and $St = 0.20$ as it was suggested from the experiment.

4.2.2. Natural Frequencies

The natural frequencies of the SCR are illustrated for the different load cases in Figure 4.9. Black lines represent the ones as measured from the experiment and the red dots represent the ones calculated numerically for current velocity of $0.07 m/s$. The natural frequencies decrease with an increasing incident flow because the current flow hits the outer part of the catenary riser and decreases the tension in the cable.

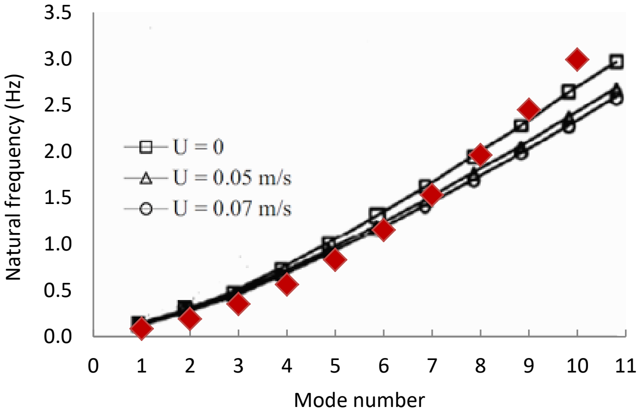

Figure 4.9: Natural frequencies of the SCR; black lines as measured from the experiment, red dots as calculated in OrcaFlex for 0.07m/s

4.2.3. Results

In this section numerous results for the load case of $0.07 m/s$ are presented. The results of $0.05 m/s$ are very similar to the ones of $0.07 m/s$ and they have been omitted.

Static

In Figure 4.10a the inclination angle along the riser length during static configuration (including the current effect) is illustrated. The top node has an inclination angle of 20° as in the experiment and the angle is increasing along the riser length due to the catenary shape. The vortex shedding frequency varies along the SCR length because the normal component of the flow velocity depends on the inclination angle. As the inclination angle increases the normal component of flow velocity decreases, thus resulting in smaller vortex shedding frequency values.

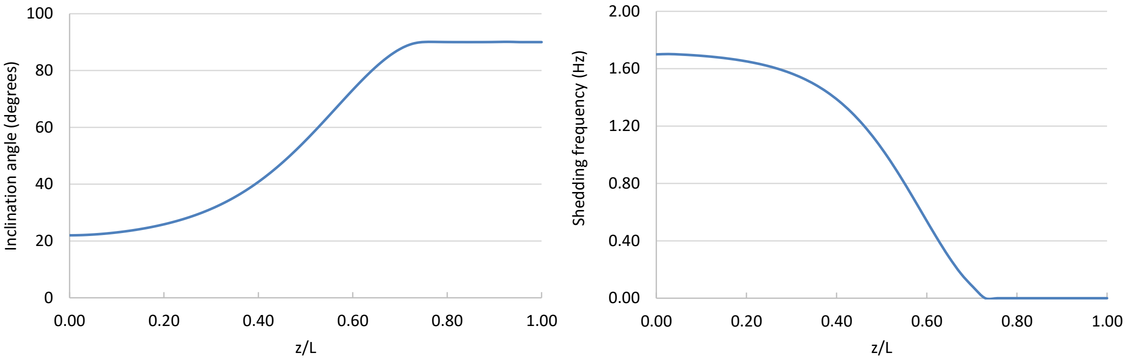

(a) (b)

Figure 4.10: (a) Inclination angle and (b) vortex shedding frequency variation along the riser length

Spectral Densities

In Figure 4.11a the dominant frequency of the crossflow vibrations for a node at $4.8m$ as calculated from numerical simulations can be seen. In the same figure are also included the first 10 natural frequencies of the riser. The riser vibrates at the frequency of 1.5 Hz which is close to the 7th mode shape. In Figure 4.11b the crossflow vibration envelope is illustrated, which confirms that the riser is vibrating in the 7th mode shape. The numerical analysis showed that the whole riser vibrates at the same frequency of 1.5 Hz. Vibration at a frequency around 1.5 Hz was expected since the top 35% of the riser (where the normal velocity is higher due to the inclination angle, thus the energy input from the wakes to the riser is higher) has a shedding frequency from 1.5 to 1.7 Hz (4.10b).

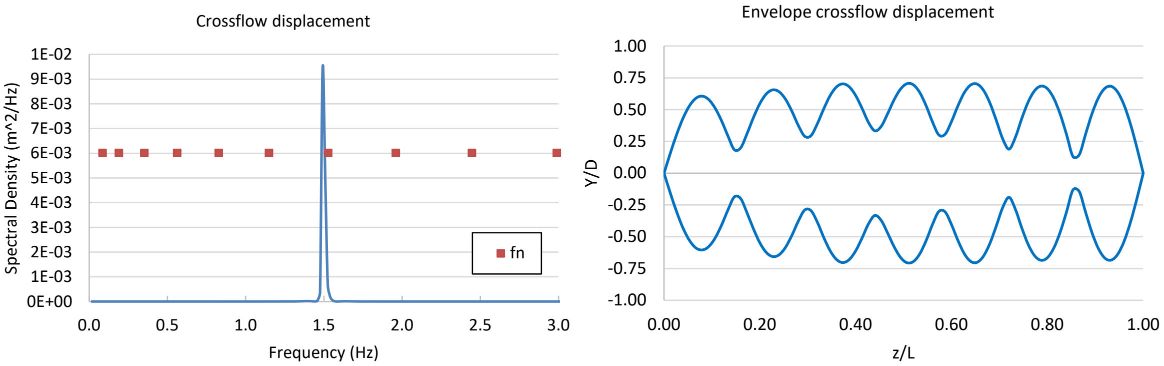

(a) (b)

Figure 4.11: Crossflow displacement (a) spectral density (b) envelope from numerical simulations

The dominant frequencies for the crossflow vibrations along the riser length as measured from the experiment are illustrated in Figure 4.12. The frequencies were 1.43 Hz (dominant), 1.35 Hz and 1.25 Hz. The results of the experiment and the simulations demonstrate sufficient agreement.

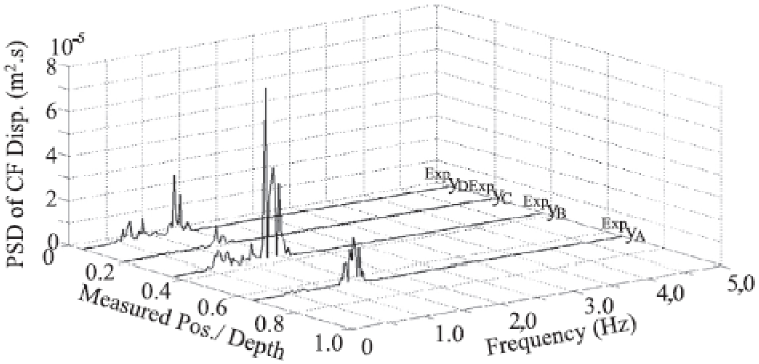

Figure 4.12: Spectral density of crossflow displacement from the experiment

As expected the dominant frequency for in-line vibrations is twice the crossflow vibration frequency at approximately 3 Hz (Figure 4.13). The same results were obtained in the experiment in which they observed that the peak frequency in the PSD of in-line acceleration is twice that of the crossflow acceleration.

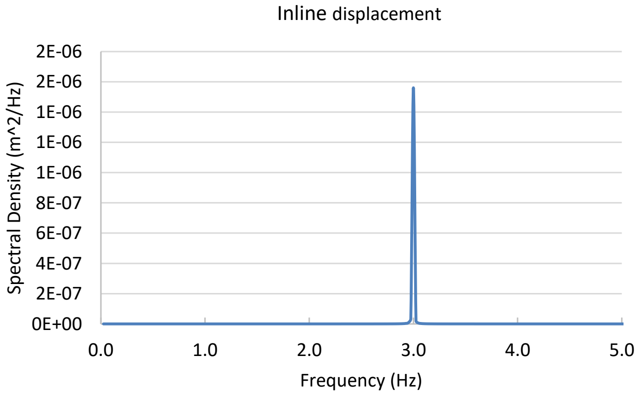

Figure 4.13: Spectral density of in-line displacement

Tension results

The numerical results (Figure 4.14a) showed that the dominant frequency of the top tension is the same with the one from the in-line displacement equal with 3 Hz. The experimental results (Figure 4.14a) showed vibrations at the dominant frequencies of both the in-line and crossflow direction. This is attributed to the load cell setup in the experiment and the type of sensor used. As can be seen in Figure 4.7 the load cell is free to move with the cable, as it vibrates. On the other hand in the simulations the top node is fixed.

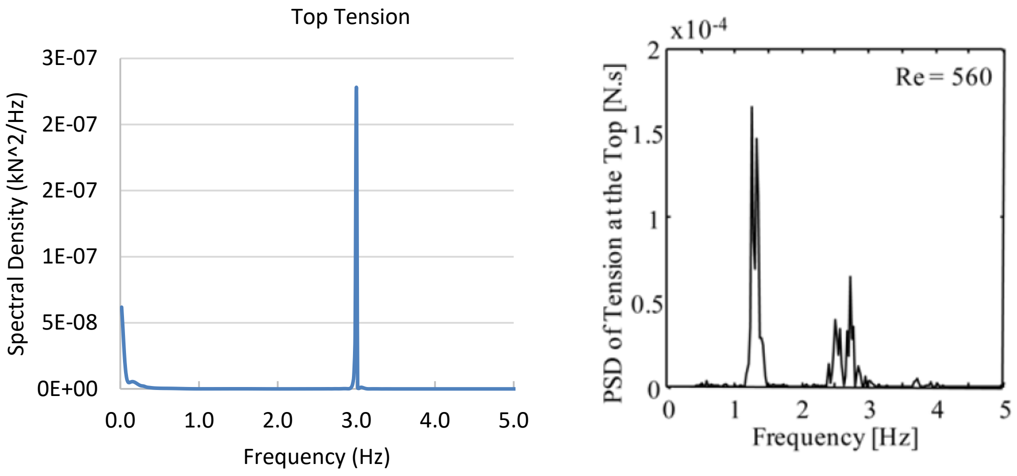

(a) (b)

Figure 4.14: Spectral density of top tension from (a) numerical simulations (b) the experiment

The dynamic part of the tension as calculated by numerical simulations and as measured from the experiment is presented in Figure 4.15a and 4.15b respectively. The static value of the tension was removed and the variables were made dimensionless by diving them with the tension measured under still water conditions. As one can observe there is good agreement in the results, in which the top tension fluctuation is approximately 6%.

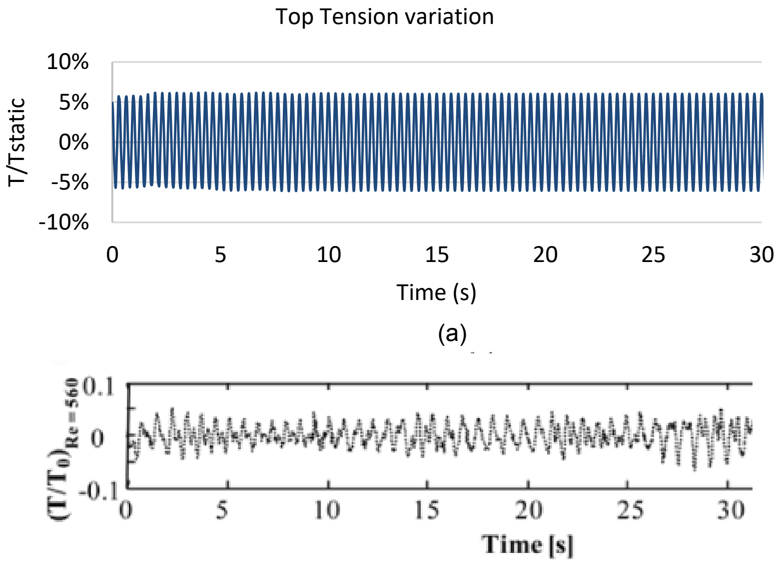

(b)

Figure 4.15: Time series of top tension from (a) numerical simulations (b) the experiment

Timeseries

The results of the simulations are in a good agreement with the experimental ones, but the amplitudes of the vibrations have been underestimated. The maximum crossflow vibration amplitude is approximately $0.75D$ (Figure 4.16a) which is smaller than the value of $1D$ (Figure 4.16b) that the experimental results showed.

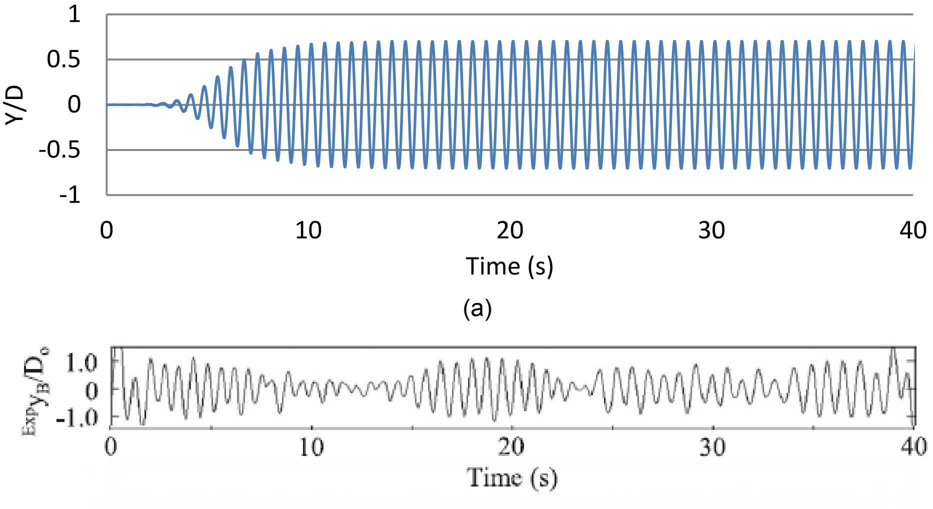

(a)

(b)

Figure 4.16: Time history of the crossflow displacement obtained (a) numerical simulations (b) the experiment at the position of the 2nd accelerometer

The motion trajectories of the vibration in the steady state regime at the position of the 2^{nd} accelerometer are illustrated in the following figure. The characteristic “figure-eight” trajectory occurs because the in-line vibration frequency is double the crossflow vibration frequency and the phase difference between the in-line and the crossflow displacement [Triantafyllou et al., 2016].

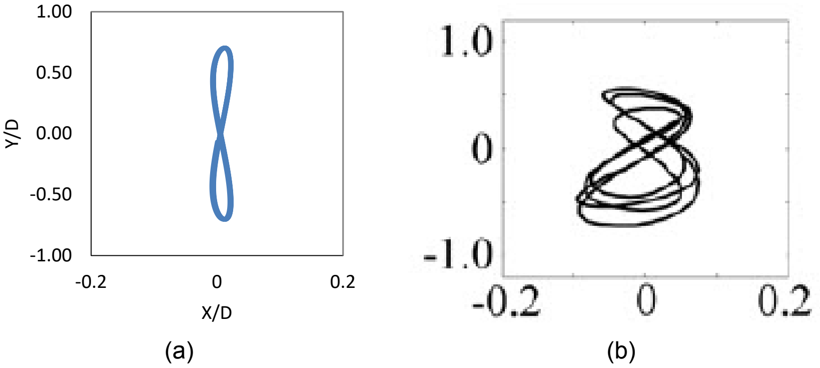

(a)

(b)

Figure 4.17: Motion trajectories of (a) numerical simulations (b) the experiment at the position of the 2nd accelerometer

Remarks:

• The simulations showed lock-in in the frequency of 1.5Hz, although the experimental results showed multifrequency response (dominant 1.43HZ). Therefore in the timehistory of the crossflow vibrations there is beating behavior in the results of the measurements, which is absent in the simulation results.

• Overall, the model predicts well the dominant vibration frequency.

• The model underestimated the maximum amplitude of the crossflow vibrations ($0.75D$ instead of $1D$.

• There are no available results from the experiment in terms of in-line displacements, thus no conclusions can be drawn.

4.3. Comparison with Milan wake oscillator model

In this section a comparison between the Milan wake oscillator model from OrcaFlex and the model used in this thesis, WOM(A=10 ϵ=0.07), is presented. Details about OrcaFlex's VIV models can be found in Appendix H. The Milan model is used because according to [Isherwood, 2007a] is more accurate than the rest. The latter is also confirmed from results that can be found in section B.0.1, Appendix B.

4.3.1. Delft Flume experiment

In Figures 4.18a, 4.19a and 4.20a the crossflow displacement envelope is illustrated for the Milan model and WOM(A=10 ϵ=0.07) for three loadcases. The results of the two models are in a very good agreement in terms of crossflow vibrations frequencies and vibration amplitudes.

As regards the envelope of in-line displacement (Figures 4.18b, 4.19b and 4.20b) one can notice significant differences between the two models. The Milan model is not capable of predicting in-line drag amplification due to VIV. Therefore the in-line displacement that is illustrated in the graph it is a result of the standard Morison drag term.

- ***Case*** **3**

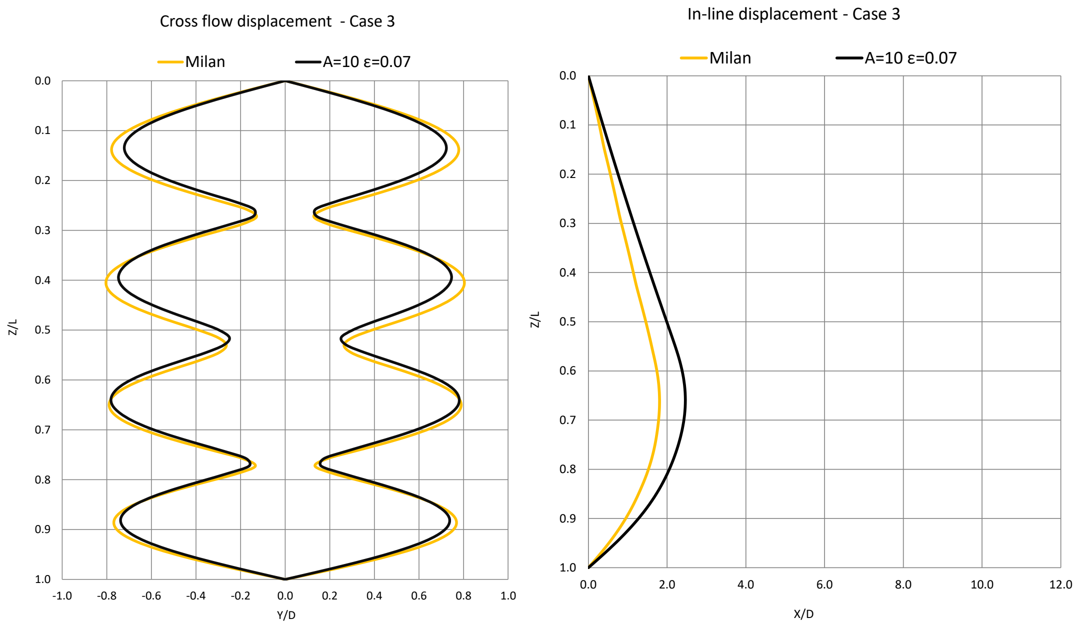

(a) (b)

Figure 4.18: Case 3-Envelope (a) crossflow (b) in-line displacement - Milan model & WOM(A=10 ϵ=0.07)

- ***Case 6***

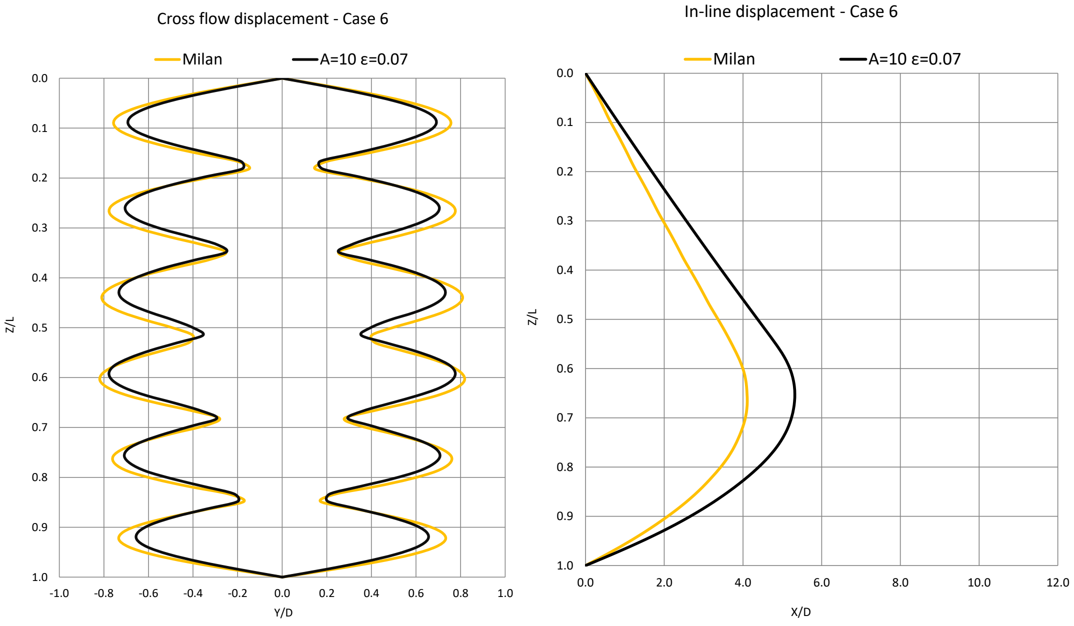

(a) (b)

Figure 4.19: Case 6-Envelope (a) crossflow (b) in-line displacement - Milan model & WOM(A=10 ϵ=0.07)

- ***Case 9***

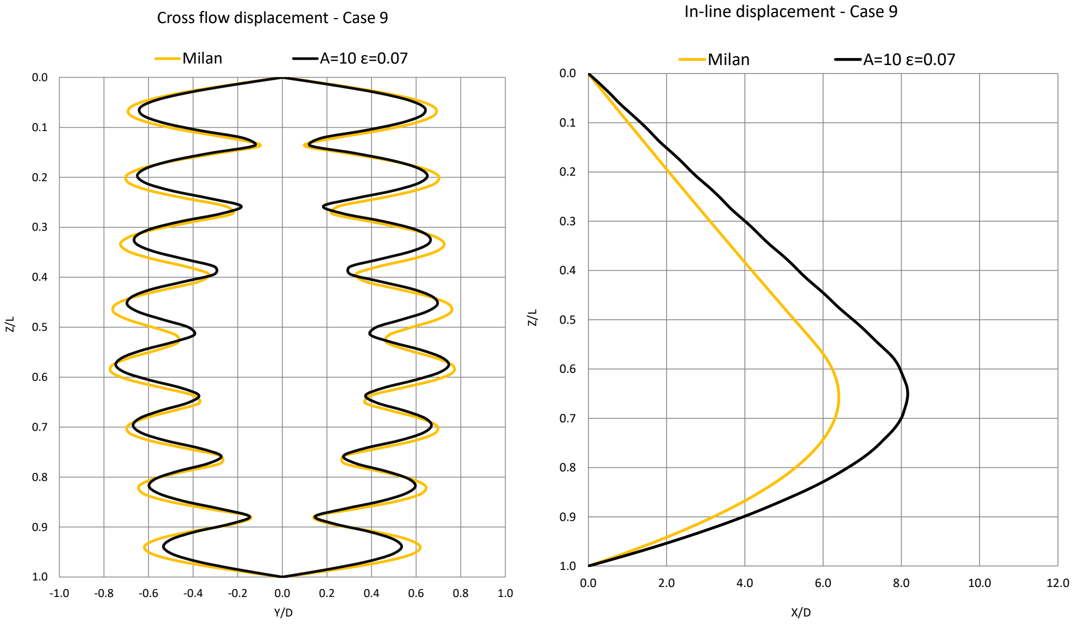

(a) (b)

Figure 4.20: Case 9-Envelope (a) crossflow (b) in-line displacement - Milan model & WOM(A=10 ϵ=0.07)

4.3.2. São Paulo experiment

In Figure 4.21 the crossflow vibration envelope can be seen for the two models. Milan model predicted vibrations in the 6^{th} mode shape and WOM(A=10 ϵ=0.07) predicted vibrations in the 7^{th}. The maximum amplitude of vibrations predicted by Milan model is slightingly smaller.

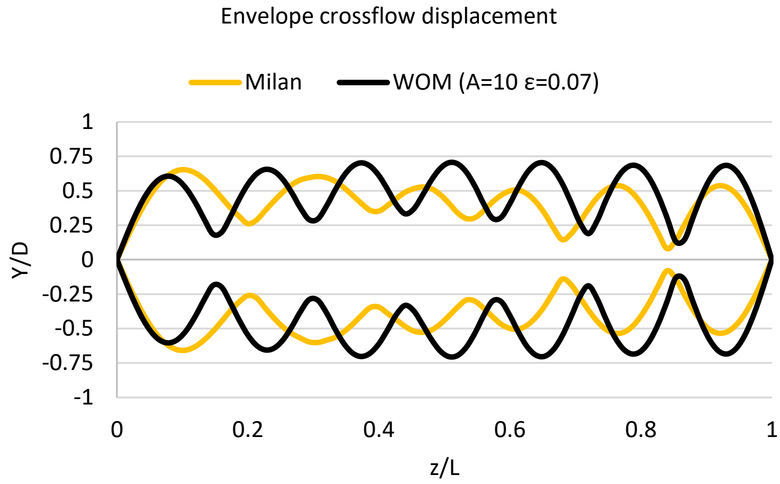

Figure 4.21: Envelope crossflow displacement - Milan model and WOM(A=10 ϵ=0.07)

As already discussed, the Milan model is not capable of predicting the in-line drag amplification. Looking in Figure 4.23 where the envelope of the in-line displacement due to VIV along the riser's length is illustrated (the in-line displacement due to the standard Morison term has been subtracted), one can observe the difference between the two models. In the case of Milan model the small in-line displacement is a result of the crossflow displacement because of the 3D geometry of the riser (crossflow vibrations affect the position of the nodes in the X direction as well). In the case of WOM(A=10 ϵ=0.07) the riser finds a new equilibrium position and the vibrations are taking place around this position. The above mentioned is becoming more evident if one observes the in-line displacement at a specific node (Figure 4.22).

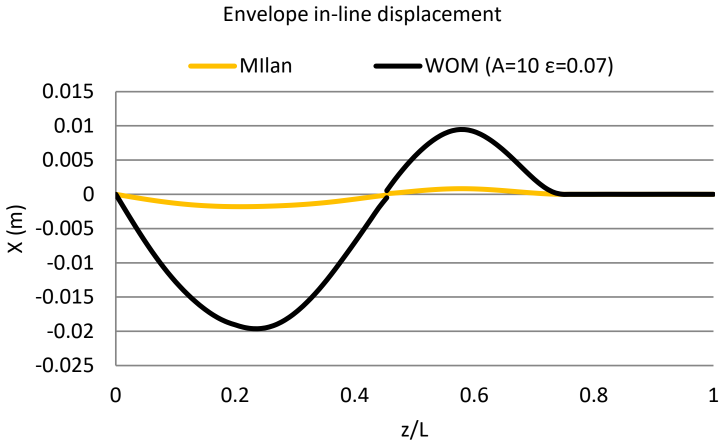

Figure 4.22: Envelope in-line displacement - Milan model and WOM(A=10 ϵ=0.07)

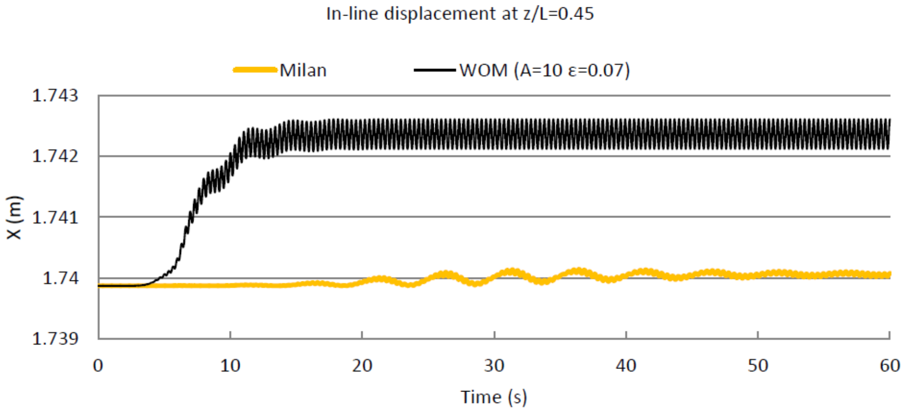

Figure 4.23: In-line displacement at z/L=0.45 - Milan model, WOM(A=10 ϵ=0.07)

The incapability of OrcaFlex's model to predict in-line displacements as seen in the above graphs, results in incapability to predict the correct tension fluctuations due to VIV. In Figure 4.24 where the top tension timeseries is illustrated, one can clearly see the difference in the calculated tensions.

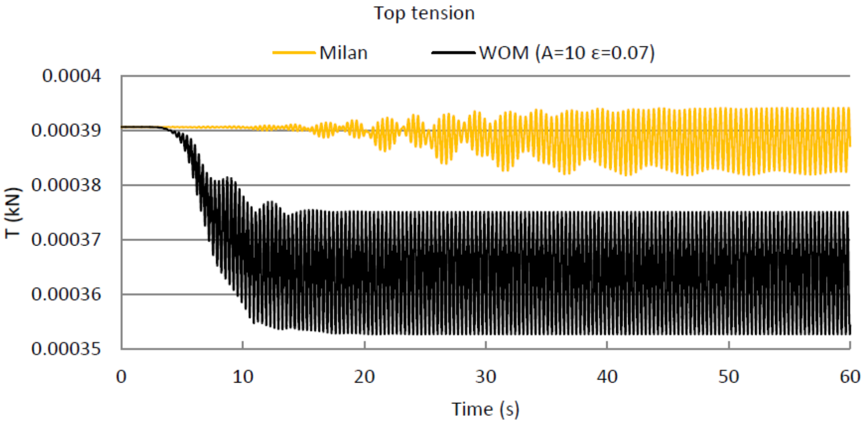

Figure 4.24: Top tension timeseries - Milan model and WOM(A=10 ϵ=0.07)

4.4. Chapter summary

In this chapter the couple structure-wake oscillator model was successfully validated against experimental data. The model is capable of capturing accurately the dominant frequency of vibrations. Regarding the amplitude of the crossflow vibrations there is an underestimation in the case of catenary shaped riser.

The results of the model were also compared with the Milan wake oscillator model from OrcaFlex's VIV models. The comparison showed that in terms of crossflow frequency and vibrations the Milan model has is in a very good agreement with the model presented in this thesis. Although the Milan model incapable to predict in-line drag amplification due to VIV and thus results in incorrect tension fluctuations. Therefore the model WOM(A=10 ϵ=0.07) is considered superior in comparison with OrcaFlex's VIV models.

The next step is to perform VIV analysis using our model in real life projects. At the next chapter a case study is examined.

5

CASE STUDY

The content of this chapter is confidential

5.1. Project

5.2. Model description

5.3. Conventions and definitions

5.4. Loadcases

5.5. Static

5.6. Direction 0°

5.6.1. Case A1 - Vtop=0.5m/s

5.6.2. Case A2 - Vtop=1.5m/s

5.6.3. Case A3 - Vtop=3.0m/s

5.7. Direction 180°

5.7.1. Case B1 - Vtop=0.5m/s

5.7.2. Case B2 - Vtop=1.5m/s

5.8. Direction 90°

5.8.1. Case C1 - Vtop=0.5m/s

5.8.2. Case C2 - Vtop=1.5m/s

5.9. Chapter summary

6

CONCLUSIONS & RECOMMENDATIONS

6.1. Conclusions

In this thesis a wake-structure model was created based on the wake oscillator model. The structure was modeled in the finite element software OrcaFlex and the wake model was created in the programming language Python. The model was assessed using the experimental data of two VIV experiments ,namely, Delft Flume experiment and São Paulo experiment. The model was also compared with the Milan wake oscillator model from OrcaFlex's VIV models.

From the validation of the model the following conclusions can be drawn:

- The model captures well the dominant vibration mode.

- The set of tuning parameters based on 2DOF fitting (A=10 ϵ=0.07) achieves results (both crossflow and in-line displacements) closer to the experimental ones than the set of tuning parameters based on 1DOF fitting (A=4 ϵ=0.05 and A=12 ϵ=0.7).

- The model estimates well the amplitude of crossflow vibrations for straight cylinders. For catenary shaped risers there is a small underestimation.

- The in-line displacement is underestimated. Although, the underestimation is smaller than 50% that [Slingsby, 2015] and [Mina, 2013] stated in their studies. The main difference in the results of the current study and their research is attributed to the modeling of the boundary conditions.

- The model presented in this thesis is superior than the Milan wake oscillator model (the Milan model is considered the most accurate among the OrcaFlex's VIV models). The two models are in a very good agreement regarding the vibration frequency and crossflow amplitudes, but the Milan model is incapable to predict in-line drag amplification thus in-line displacements due to VIV.

From the results of the case study the following conclusions can be drawn:

The content of this section is confidential

6.2. Recommendations

General

The wake-structure model should be assessed against more experimental/real world results for catenary shaped structures (cables, risers, etc.). More comparisons are needed thus more solid conclusions can be extracted regarding the suitability of the model for catenary shaped structures.

If a more precise calculation of the tension due to VIV is needed then a model which can predict better the in-line drag amplification should be searched for. To the author's knowledge the model used in this thesis is the best model available up to date.

In this study VIV due to steady current was examined. It is suggested to investigate the effect of waves on the VIV.

Furthermore, the effect of vessel motions on the VIV should be examined. In this research the vessel was considered stationary.

Operational

The content of this section is confidential

Bibliography

G. R. S. Assi, N. Srinil, C. M. Freire, and I. Korkischko. Experimental investigation of the flow-induced vibration of a curved cylinder in convex and concave configurations. *Journal of Fluids and Structures*, 44:52–66, 2014. doi: 10.1016/j.jfluidstructs.2013.10.011.

R. D. Blevins. *Flow-Induced Vibration*. Krieger Publishing Company, second edition, 1990.

R. D. Blevins and C. S. Coughran. Experimental Investigation of Vortex-Induced Vibration in One and Two Dimensions With Variable Mass, Damping, and Reynolds Number. *Journal of Fluids Engineering*, 131(10):101202, 2009. ISSN 00982202. doi: 10.1115/1.3222904. URL `http://fluidsengineering.asmedigitalcollection.asme.org/article.aspx?articleid=1478300`.

J. R. Chaplin, P. W. Bearman, Y. Cheng, E. Fontaine, J. M. R. Graham, K. Herfjord, F. J. Huera Huarte, M. Isherwood, K. Lambrakos, C. M. Larsen, J. R. Meneghini, G. Moe, R. J. Pattenden, M. S. Triantafyllou, and R. H. J. Willden. Blind predictions of laboratory measurements of vortex-induced vibrations of a tension riser. *Journal of Fluids and Structures*, 21(1 SPEC. ISS.):25–40, 2005a. ISSN 08899746. doi: 10.1016/j.jfluidstructs.2005.05.016.

J. R. Chaplin, P. W. Bearman, F. J. Huera Huarte, and R. J. Pattenden. Laboratory measurements of vortex-induced vibrations of a vertical tension riser in a stepped current. *Journal of Fluids and Structures*, 21(1 SPEC. ISS.):3–24, 2005b. ISSN 08899746. doi: 10.1016/j.jfluidstructs.2005.04.010.

J. Chung and G. M. Hu. A Time Integration Algorithm for Structural Dynamics With Improved Numerical Dissipation-The Generalized-α Method. *ASME Journal of Applied Mechanics.*, 60: 371–375, 1993.

M. L. Facchinetti, E. de Langre, and F. Biolley. Coupling of structure and wake oscillators in vortex-induced vibrations. *Journal of Fluids and Structures*, 19(2):123–140, 2003. doi: 10.1016/j.jfluidstructs.2003.12.004.

M. L. Facchinetti, E. De Langre, and F. Biolley. Vortex-induced travelling waves along a cable. *European Journal of Mechanics, B/Fluids*, 23(1):199–208, 2004. ISSN 09977546. doi: 10.1016/j.euromechflu.2003.04.004.

M. Falco, F. Fossati, and F. Resta. On the vortex induced vibration on submarine cables:design optimization of wrapped cables for controlling vibrations. pages 3–8, Trondheim, Norway, 1999. 3rd International Symposium on Cable Dynamics.

R. M. Isherwood. R648#01#02 OrcaFlex VIV Validation Summary. Technical Report September, 2007a.

R. M. Isherwood. R648#03#02 OrcaFlex VIV Comparison with Schiehallion Results. Technical Report September, 2007b.

R. M. Isherwood. R648#04#02 OrcaFlex VIV Comparison with Deepstar Seneca Trials. Technical Report September, 2007c.

R. M. Isherwood. R648-02-02 OrcaFlex VIV Comparison with Delft Model Tests. Technical Report September, 2007d.

W. D. Iwan and R. D. Blevins. A Model for Vortex Induced Oscillation of Structures. *Journal of Applied Mechanics*, 41(3):581, 1974. ISSN 00218936. doi: 10.1115/1.3423352.

A. Jain and Y. Modarres-Sadeghi. Vortex-induced vibrations of a flexibly-mounted inclined cylinder. *Journal of Fluids and Structures*, 43:28–40, 2013. ISSN 08899746. doi: 10.1016/j.jfluidstructs.2013.08.005. URL `http://dx.doi.org/10.1016/j.jfluidstructs.2013.08.005`.

N. Jauvtis and C. H. K. Williamson. Vortex-induced vibration of a cylinder with two degrees of freedom. *Journal of Fluids and Structures*, 17(7):1035–1042, 2003. doi: 10.1016/S0889-9746(03)00051-3.

A. Khalak and C. Williamson. Motions, Forces and Mode Transitions in Vortex-Induced Vibrations At Low Mass-Damping. *Journal of Fluids and Structures*, 13(7-8):813–851, 1999. ISSN 08899746. doi: 10.1006/jfls.1999.0236. URL `http://www.sciencedirect.com/science/article/pii/S0889974699902360`.

A. Miliou, S. J. Sherwin, J. Michael, and R. Graham. Fluid Dynamic Loading on Curved Riser Pipes. *ASME Journal Of Offshore Mechanics and Arctic Engineering*, 125:176–182, 2003. doi: 10.1115/1.1576817□.

A. Mina. Modeling the vortex-induced vibrations of a multi-span free standing riser. *Master's thesis, Delft University of Technology*, 2013.

C. K. Morooka and R. I. Tsukada. Experiments with a steel catenary riser model in a towing tank. *Applied Ocean Research*, 43:244–255, 2013. ISSN 01411187. doi: 10.1016/j.apor.2013.10.010. URL `http://dx.doi.org/10.1016/j.apor.2013.10.010`.

R. H. M. Ogink and A. V. Metrikine. A wake oscillator with frequency dependent coupling for the modeling of vortex-induced vibration. *Journal of Sound and Vibration*, 329(26):5452–5473, 2010. ISSN 0022460X. doi: 10.1016/j.jsv.2010.07.008. URL `http://dx.doi.org/10.1016/j.jsv.2010.07.008`.

Orcina. OrcaFlex Manual. Technical Report Version 9.1a, 2014.

T. Sarpkaya. A critical review of the intrinsic nature of vortex induced vibrations. *Journal of Fluids and Structures*, 19(June):389–447, 2003.

M. Slingsby. Dynamic Interaction of Subsea Pipeline Spans due to Vortex-Induced Vibrations. *Master's thesis, Delft University of Technology*, 2015.

J. Sun. Scale test facility for measuring vortex induced vibrations. *Master's thesis, Delft University of Technology*, 2017.

M. S. Triantafyllou, R. Bourguet, J. Dahl, and Y. Modarres-Sadeghi. Vortex-induced vibrations. In *Springer Handbook of Ocean Engineering*. 2016. ISBN 9783319166490. doi: 10.1007/978-3-319-16649-0{_}36.

Vandiner J.K. Drag Coefficients of Long-Flexible cylinders. Houston, May 2-5, 1983. Offshore Technology Conference.

K. Vikestad, J. Valdiver, and C. Larsen. Added mass and oscillation frequency for a circular cylinder subjected to vortex-induced vibrations and external disturbance. *Journal of Fluids and Structures*, 14:1071–1088, 2000.

A

Van der Pol oscillator

The wake oscillator is a modified Van Der pol equation and reads as:

$$\ddot{q} + \epsilon\omega_s(q^2 - 1)\dot{q} + \omega_s^2 q = F(t) \tag{A.1}$$

Where:	q	is the wake variable [-]
	ϵ	is a tuning parameter [-]
	ω_s	is the natural frequency of the oscillator $[rad/s]$
	$F(t)$	is the forcing term

In this section various values will be used in the Van der Pol equation in order to illustrate how it works and extract some conclusions. For all the cases the forcing term is equal to F(t)=A cos(ω_f t) where, A is a tuning parameter [-] and ω_f is the forcing frequency $[rad/s]$.

Case 1: Unforced, $A = 0.0,\ \varepsilon = 0.1,\ q_0 = 0.01,\ q_0' = 0.0,\ \omega_s = 2\ rad/s$

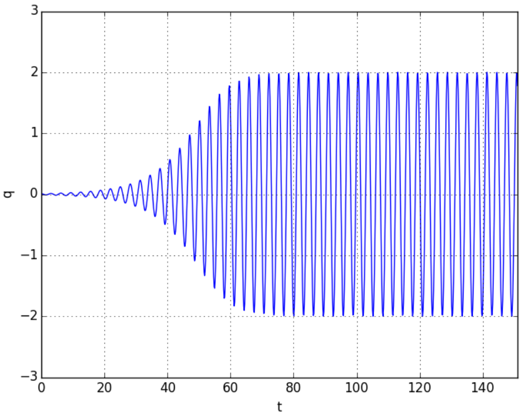

Figure A.1: Wake variable q - Case 1

In Case 1 and Case 2 the Van der Pol oscillator is unforced (A=0.0) and only the tuning parameter ε differs. One can observe that:
- the maximum steady state amplitude is $q_{max} = \pm 2$.
- the bigger the tuning parameter ε, the faster the steady state response is reached.

Case 2: Unforced, $A = 0.0,\ \varepsilon = 1.0,\ q_0 = 0.01,\ q_0' = 0.0,\ \omega_s = 2\ rad/s$

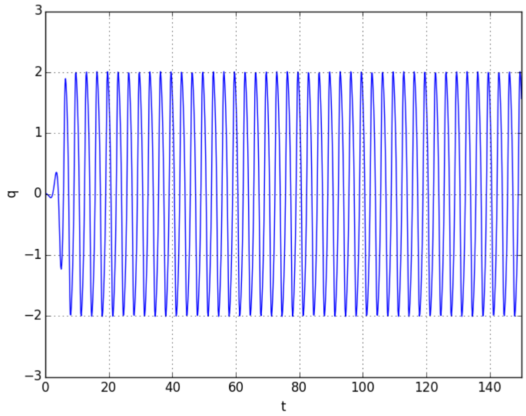

Figure A.2: Wake variable q - Case 2

In Case 3 the Van der Pol oscillator is unforced (A=0.0) and undamped (ε=0.0), thus there is no energy input or dissipation in the system and the amplitude of the oscillator depends only in the initial value of the wake variable q_0.

Case 3: Unforced, undamped, $A = 0.0,\ \varepsilon = 0.0,\ q_0 = 1.0,\ q_0' = 0.0,\ \omega_s = 0.5\ rad/s$

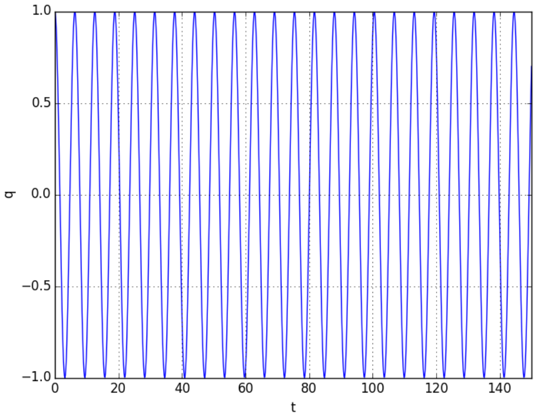

Figure A.3: Wake variable q - Case 3

In Case 4 the natural frequency of the oscillator ω_s and the frequency of the force ω_f coincide, thus the amplitude of the oscillation maximizes and its equal with $q_{max} = \pm 6$.

Case 4: $A = 5.0,\ \varepsilon = 0.1,\ q_0 = 1.0,\ q_0' = 0.0,\ \omega_s = 1.0\ rad/s,\ \omega_f = 1.0\ rad/s$

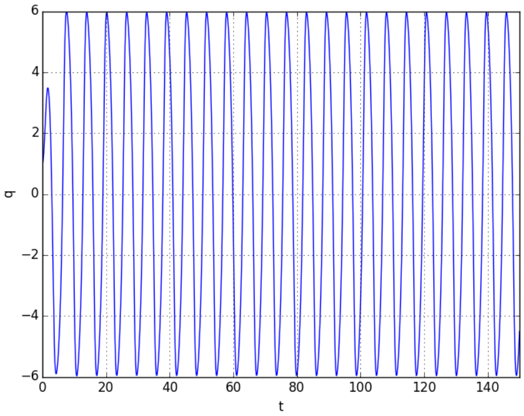

Figure A.4: Wake variable q - Case 4

Case 5 is similar to Case 4 but the tuning parameter A is larger this time. As expected the amplitude of oscillation is bigger and its equal with $q_{max} = \pm 7.2$.

Case 5: $A = 10.0,\ \varepsilon = 0.1,\ q_0 = 1.0,\ q_0' = 0.0,\ \omega_s = 1.0\ rad/s,\ \omega_f = 1.0\ rad/s$

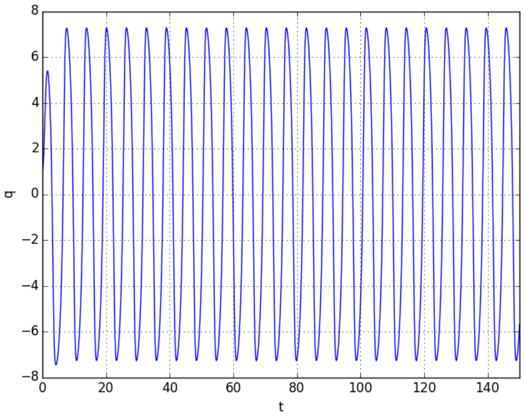

Figure A.5: Wake variable q - Case 5

Case 6 is similar to Case 4 but the forcing frequency ω_f is larger than the natural frequency of the oscillator ω_s and the maximum amplitude at the steady state regime is smaller and equal with $q_{max} = \pm 5.8$.

Case 6: $A = 5.0,\ \varepsilon = 0.1,\ q_0 = 1.0,\ q_0' = 0.0,\ \omega_s = 0.5\ rad/s,\ \omega_f = 1.0\ rad/s$

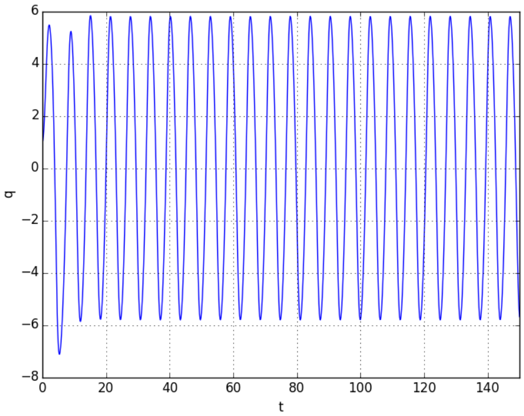

Figure A.6: Wake variable q - Case 6

Case 7 is similar to Case 4 but the forcing frequency ω_f is smaller than the natural frequency of the oscillator ω_s and the maximum amplitude at the steady state regime is also smaller and equal with $q_{max} = \pm 5.6$.

Case 7: $A = 5.0,\ \varepsilon = 0.1,\ q_0 = 1.0,\ q_0' = 0.0,\ \omega_s = 1.0\ rad/s,\ \omega_f = 0.5\ rad/s$

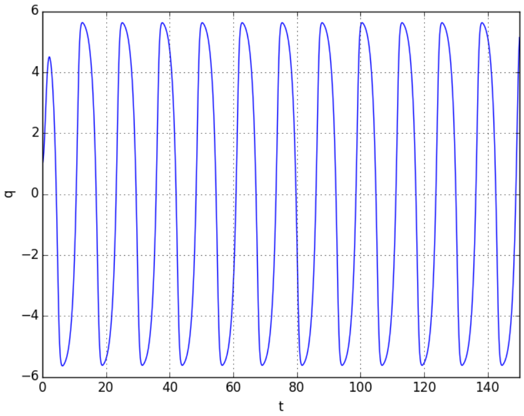

Figure A.7: Wake variable q - Case 7

B

Delft Model Tests

Spectral density of crossflow and in-line vibrations

In this section results in terms of spectral frequencies are presented for the 3 loadcases of Delft flume experiment. In the Figures on the left side, the crossflow vibration frequency can be seen, along with the natural frequencies and shedding frequency. In each graph spectral densities for the 3 sets of tuning parameters are illustrated. In Figures on the right side the in-line vibration frequency is presented, again for 3 sets of tuning parameters. One can observe that the in-line vibration frequency is double the crossflow one, as expected.

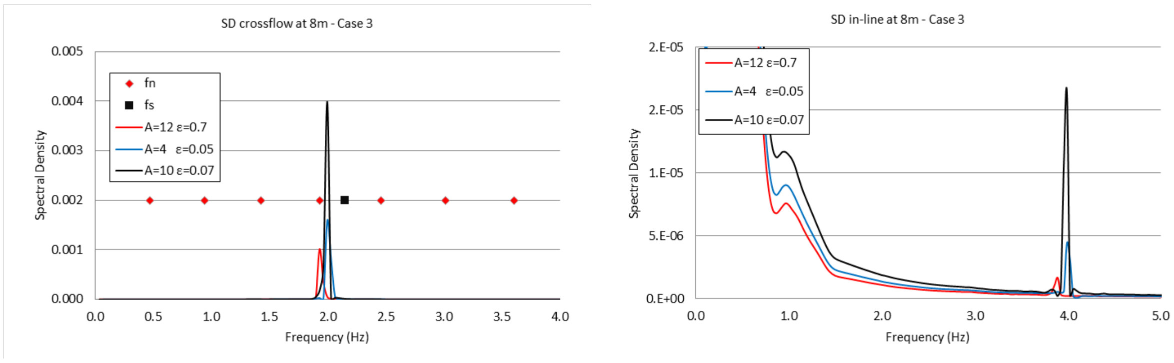

(a) (b)

Figure B.1: Case 3-Spectral density of (a) crossflow (b) in-line displacement

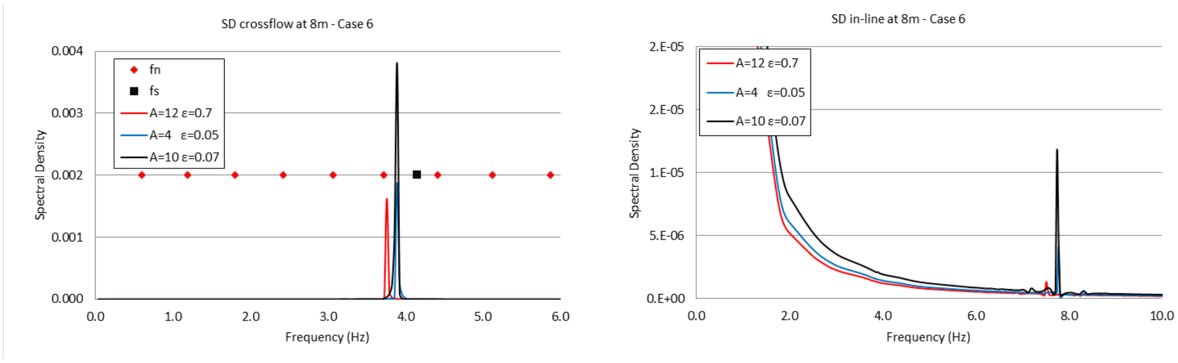

(a) (b)

Figure B.2: Case 6-Spectral density of (a) crossflow (b) in-line displacement

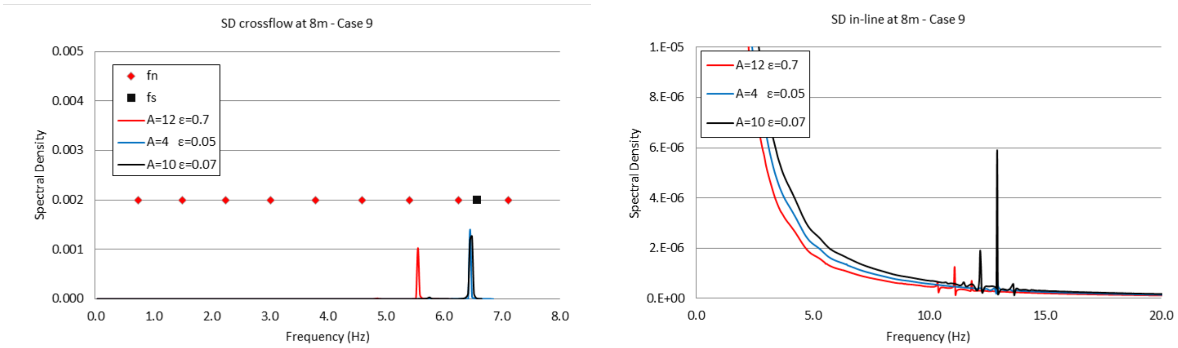

(a) (b)

Figure B.3: Case 9-Spectral density of (a) crossflow (b) in-line displacement

Timeseries of crossflow and in-line vibrations

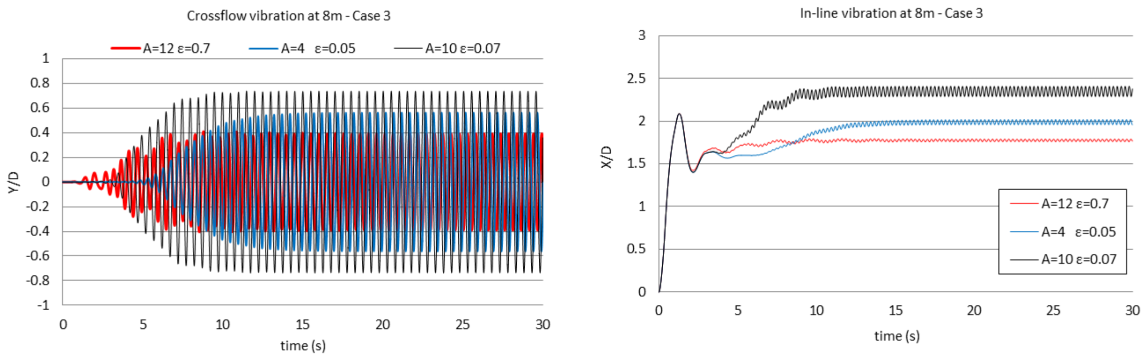

(a) (b)

Figure B.4: Case 3-Timeseries of (a) crossflow (b) in-line displacement

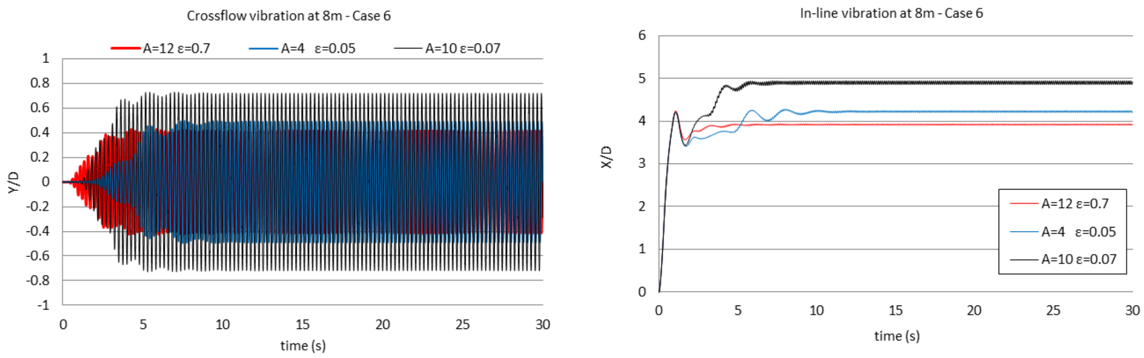

(a) (b)

Figure B.5: Case 6-Timeseries of (a) crossflow (b) in-line displacement

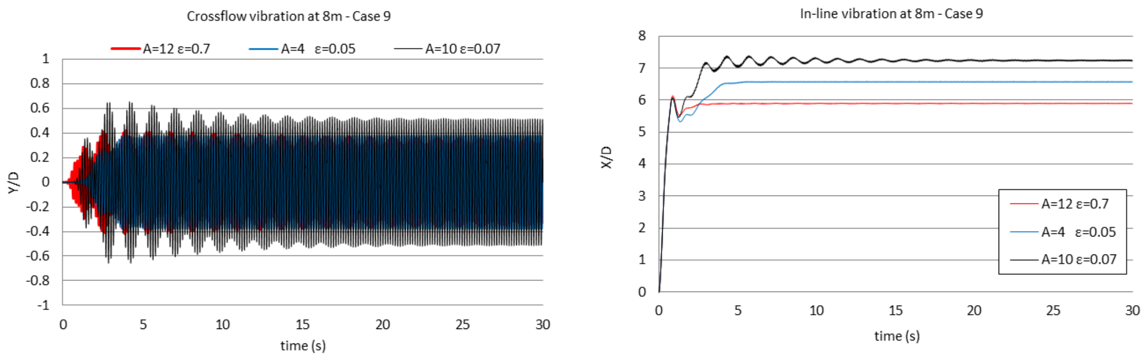

(a) (b)

Figure B.6: Case 9-Timeseries of (a) crossflow (b) in-line displacement

B.0.1. OrcaFlex's VIV models

In Figures B.7a B.8a and B.9a (figures on the left side) the results of the simulations for the Delft flume experiment using OrcaFlex's oscillator models can be seen. The Iwan&Blevins model and the Milan model was used (more information can be found in Appendix H). The results from Milan model are in good agreement with the experimental ones, but the results of Iwan&Blevins model show significant overestimation of the vibration amplitudes. However, both of them estimate well the dominant vibration frequency. Both models are not capable of predicting in-line drag amplification due to VIV.

In Figures B.7b B.8b and B.9b (figures on the right side) the results of the Delft flume experiment as published by Orcina in [Isherwood, 2007d] are illustrated. In their results they include three models:

- Milan wake oscillator model with as published parameters ("Milan Original")
- Milan wake oscillator model with Ca=0, other parameters as published ("Milan Ca=0")
- Iwan and Blevins wake oscillator model with as published parameters ("I+B")

The black line, namely "Measured" represents the experimental results.

One can notice that in the case of Milan model OrcaFlex's results and our simulations are in very good agreement. On the other hand, in the case of Iwan and Blevins model there is significant overestimation in the results of the simulations compared with Orcina's published results. The main reason is that Orcina has used a non default numerical damping value which lead in much smaller amplitudes.

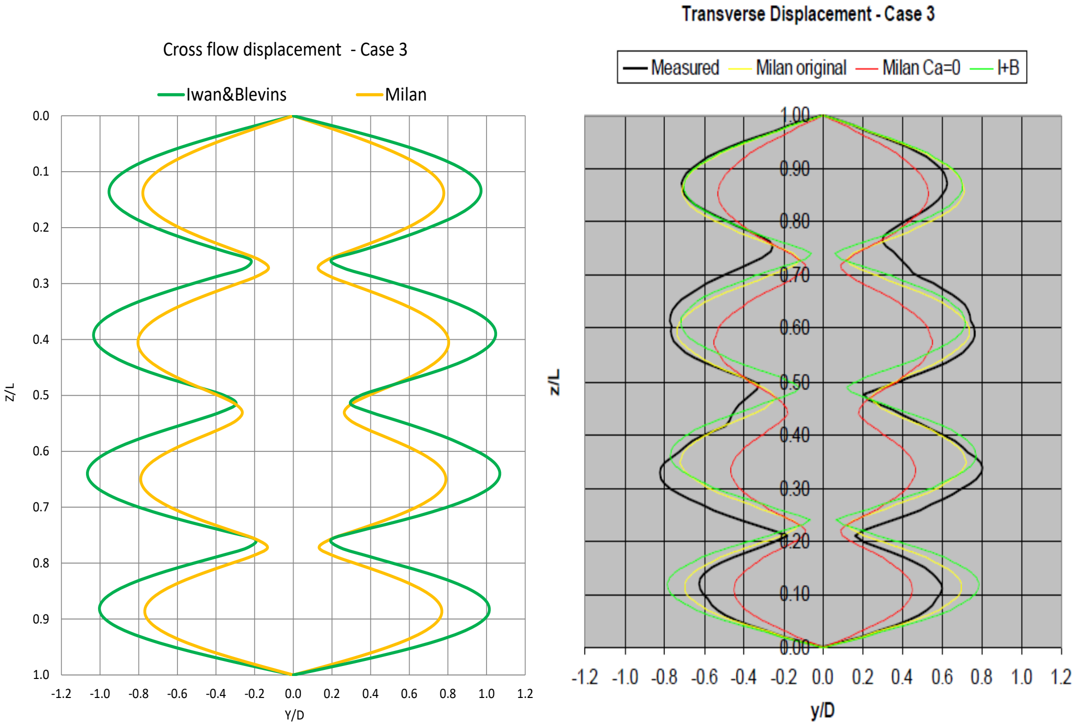

(a) (b)

Figure B.7: Envelope crossflow displacement-Case 3

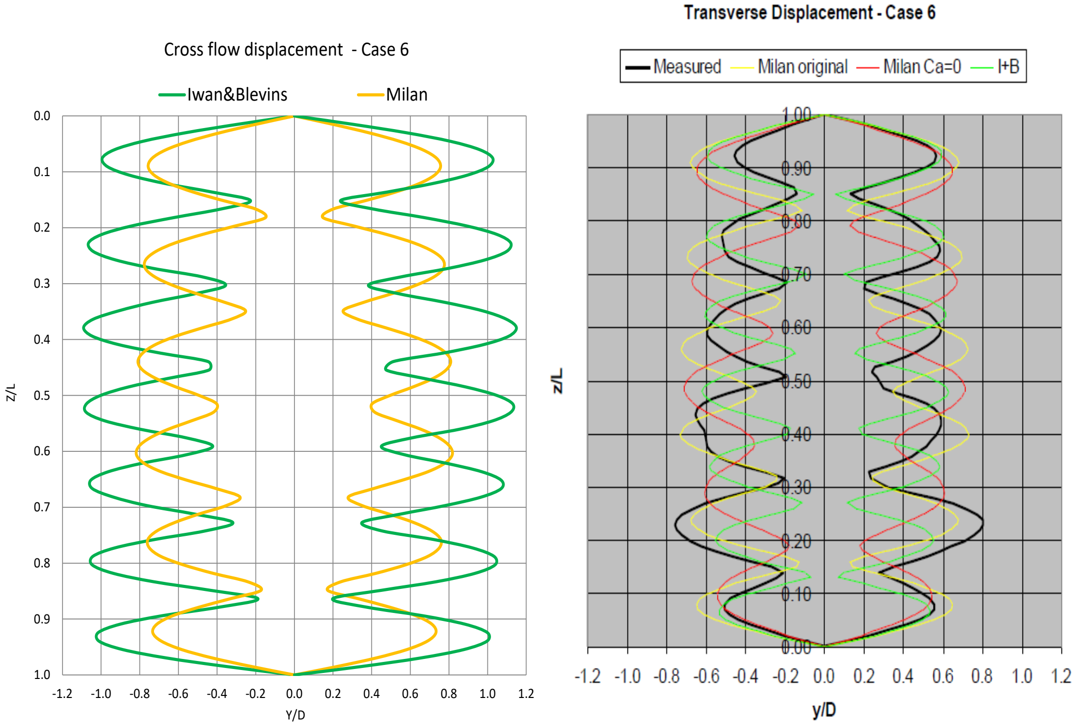

(a) (b)

Figure B.8: Envelope crossflow displacement-Case 6

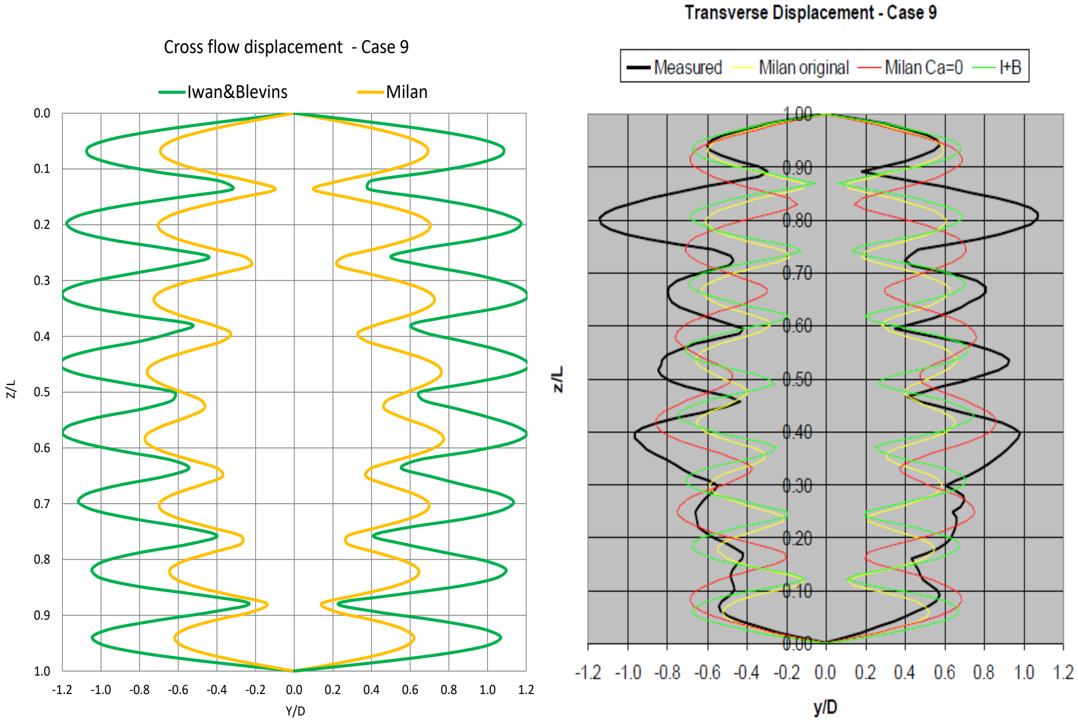

(a) (b)

Figure B.9: Envelope crossflow displacement-Case 9

C

VIV effect on Bending radius

The content of this section is confidential

D

Sensitivity analysis “Case Study”

The content of this section is confidential

E

Solution Method

OrcaFlex

I. Time domain
- Implicit Solvers
- Explicit Solvers

II. Frequency domain

Explicit Solver

Explicit methods calculate the state of the system at a later time from the properties of the system at the current time. Explicit solvers are conditionally stable which means that there must be a limit on the size of the timestep for there to be a solution. The equation of motion is formed for each free body and each line node. This is not the system-wide equation of motion, but a local equation of motion for each free body and each line node. This equation is solved for the acceleration vector at the beginning of the time step, for each free body and each line node, and then integrated using forward Euler integration. The explicit scheme used by OrcaFlex is semi-implicit Euler. This method produces an approximate discrete solution by iterating the following equations:

$$\begin{aligned} v_{n+1} &= v_n + a_n \Delta t \\ x_{n+1} &= x_n + v_{n+1} \Delta t \end{aligned} \tag{E.1}$$

The difference with the standard Euler is that the semi-implicit Euler method uses the velocity of the next time step v_{n+1} to calculate the displacement x_{n+1} at the next timestep, while the Euler method uses the velocity of the current timestep v_n.

Implicit Solver

Implicit methods find a solution by solving an equation involving both the current state of the system and the later one. Implicit solvers are unconditionally stable which means that a solution at the new timestep can be obtained for any size of timestep. Of course, the solution for very large time steps may not be realistic. OrcaFlex uses the Generalized-α integration scheme [Chung and Hu, 1993] which is unconditionally stable for linear systems. The forces, moments, damping, mass etc. are calculated in the same way as for the explicit scheme. Then the system equation of motion is solved at the end of the time step.

Remarks: Frequency domain solution cannot be used with external functions or time variable data thus they are not part of this research. Also, OrcaFlex's inbuilt VIV models can only be used only with explicit integration schemes. At the time that the VIV models were created OrcaFlex did not had implicit solvers available.

Python – Runge-Kutta (RK4)

The wake oscillator equation (modified Van Der Pol equation) is a 2^{nd} order differential equation which does not have an exact analytic solution. Thus, to solve it an ODE solver is used in the external function in python which belongs in the Runge-Kutta methods family. Specifically is based on the 4^{th} and 5^{th} order explicit Runge-Kutta method and in python it is called "dopri5".

Before evaluating the equation with the ODE solver, first we need to rewrite the 2^{nd} order differential equation to a system of two first order ODEs. It reads as follows:

$$\begin{aligned} &Wake\ oscillator\ equation: \frac{d^2q}{dt^2} + \epsilon\omega_s(q^2-1)\frac{dq}{dt} + \omega_s^2 q = F(t) \\ &Re-written\ as: \frac{dq}{dt} = y,\ \frac{dy}{dt} = -\epsilon\omega_s(q^2-1)y - \omega_s^2 q + F(t) = f(t,y) \end{aligned} \tag{E.2}$$

Now, the Runge-Kutta method approximates the latter equation as following:

$$y_{n+1} = y_n + \tfrac{\Delta t}{6}(k_1 + 2k_2 + 2k_3 + k_4)$$
$$t_{n+1} = t_n + \Delta t$$

Where:
$k_1 = f(t_n, y_n)$
$k_2 = f(t_n + \tfrac{\Delta t}{2}, y_n + \tfrac{\Delta t}{2}k_1)$
$k_3 = f(t_n + \tfrac{\Delta t}{2}, y_n + \tfrac{\Delta t}{2}k_2)$
$k_4 = f(t_n + \Delta t, y_n + \Delta t k_3)$

Thus the next value y_{n+1} is determined by the present value y_n plus the weighted average of the four increments (k_1, k_2, k_3, k_4) where the greater weight is given to the increments in the midpoint.

F

OrcaFlex-Line Theory

OrcaFlex is using finite element theory to model the Line object [Orcina, 2014]. The line is divided into a series of segments which are modeled by straight massless elements with a node at each end. Each node is effectively a short straight rod that represents two half-segments either side of the node. The segments only model the axial and torsional properties of line, the other properties (such as, mass, buoyancy,drag, etc.) are lumped to the nodes. Each node has the properties of two half segments, except from the end nodes (first and last node) that have the properties of only one half segment. A schematic representation can be seen in Figure F.1. At the location where a line segment pierces the sea surface, all forces in relation to the fluid are calculated allowing for varying wetted length up to the instantaneous water surface level.

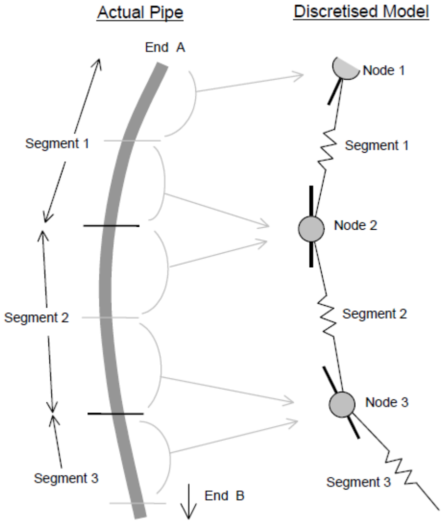

Figure F.1: OrcaFlex Line model

The axial stiffness and damping of the line are modeled by an axial spring and a damper at the center of line segment, which applies an equal and opposite effective tension force to the nodes at each end of line segment. The bending properties of the line are represented by rotational spring and dampers at each end of the segment, between the segment and the node. A more detailed representation of the Line object is given in Figure F.2.

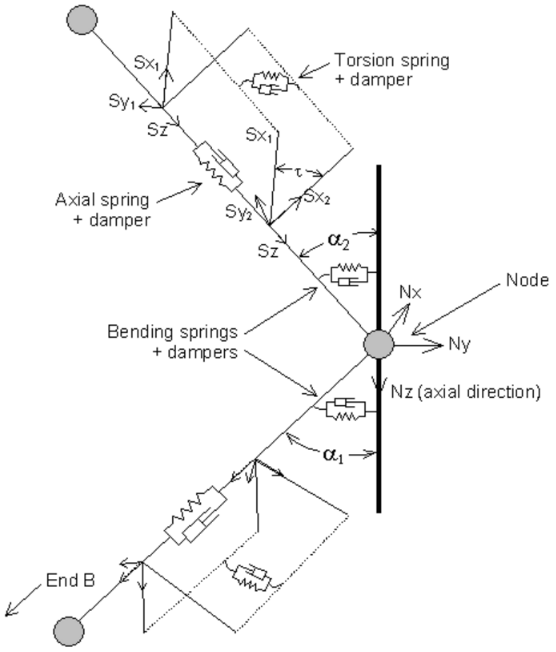

Figure F.2: Detailed Line model

If the line segment is exposed to internal and external fluid pressures the effective tension at the mid-point of line segment can be calculated as:

$$
\begin{aligned}
T_e &= T_w + (P_o A_o - P_i A_i) \\
T_w &= EA\epsilon - \nu(P_o A_o - P_i A_i) + K_{tt}\tau/L_o + EA\ C(dL/dt)/L_o
\end{aligned}
\tag{F.1}
$$

Where:	T_e	is the effective tension $[N]$
	T_w	is the wall tension $[N]$
	EA	is the axial stiffness $[N]$
	ϵ	is the total mean axial strain = $(L - \lambda L_o)/(\lambda L_o)$ $[-]$
	L	is the instantaneous length of segment $[m]$
	L_o	is the unstretched length of segment $[m]$
	λ	is the expansion factor of segment $[-]$
	ν	is the Poisson ratio $[-]$
	P_i, P_o	is the internal pressure and external pressure, respectively $[Pa]$
	A_i, A_o	is the internal and external cross sectional stress areas, respectively $[m^2]$
	K_{tt}	is the tension / torque coupling [-]
	τ	is the segment twist angle [radians]
	dL/dt	is the rate of increase of length [m/s]
	C	is the damping coefficient [s]

In this report just the term tension is used instead of the term effective tension for simplification.

Equation of Motion

The equation of motion which OrcaFlex solves is as follows:

$$M(p,\alpha) + C(p,v) + K(p) = F((p,v,t) \tag{F.2}$$

Where:	$M(p,\alpha)$	is the system inertia load
	$C(p,v)$	is the system damping load
	$K(p)$	is the system stiffness load
	$F(p,v,t)$	is the external load
	p,v and α	are the position, velocity and acceleration vectors respectively, and t is the simulation time.

G

Model fitting to experimental results

1DOF fitting - [Ogink and Metrikine, 2010]

Tuning of amplitude and frequency of oscillation of the adjusted model of [Facchinetti et al., 2003] to the measurements of [Khalak and Williamson, 1999] for: (a) $m^* = 2.4$, (b) $m^* = 10.3$ and (c) $m^* = 20.6$. Solid lines represent quantities for increasing V_n, dashed lines for decreasing V_n.

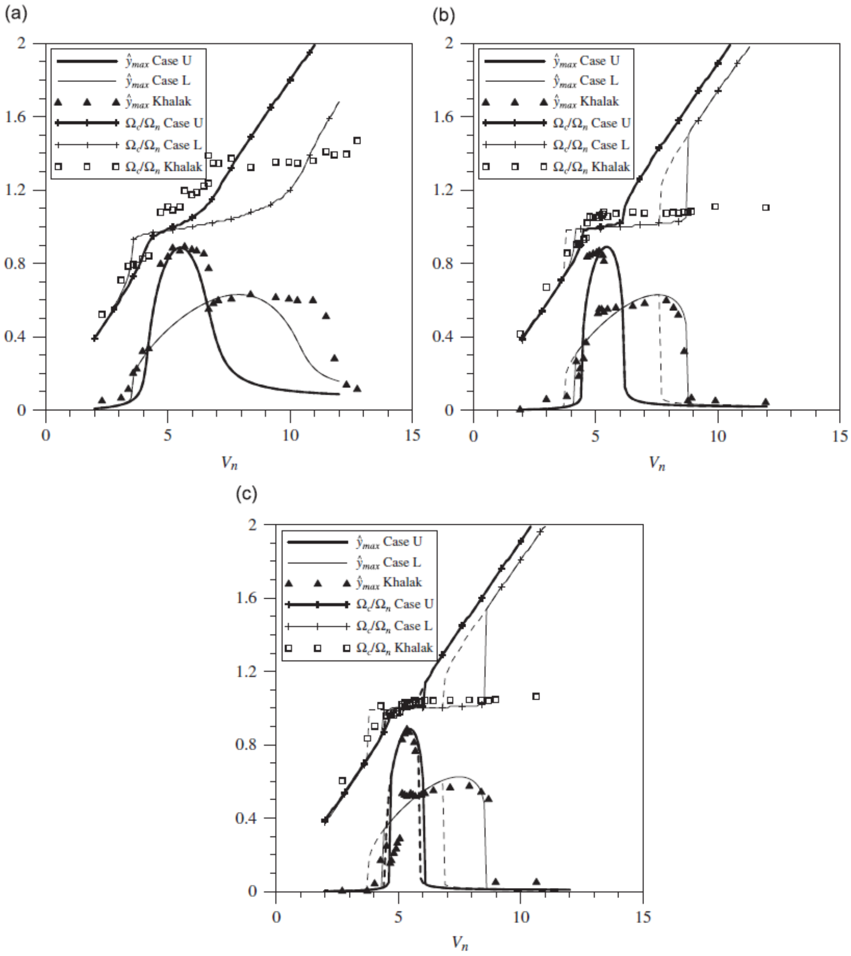

Figure G.1: Model response for A=4 and ε=0.05 and A=12 and ε=0.7 [Ogink and Metrikine, 2010]

2DOF fitting - [Slingsby, 2015]

Fitting of the tuning parameters to the measurements of [Blevins and Coughran, 2009]. For very low mass ratios the behavior changes drastically, therefore a distinction is made between two regions, with a border at a mass ratio of 1.57.

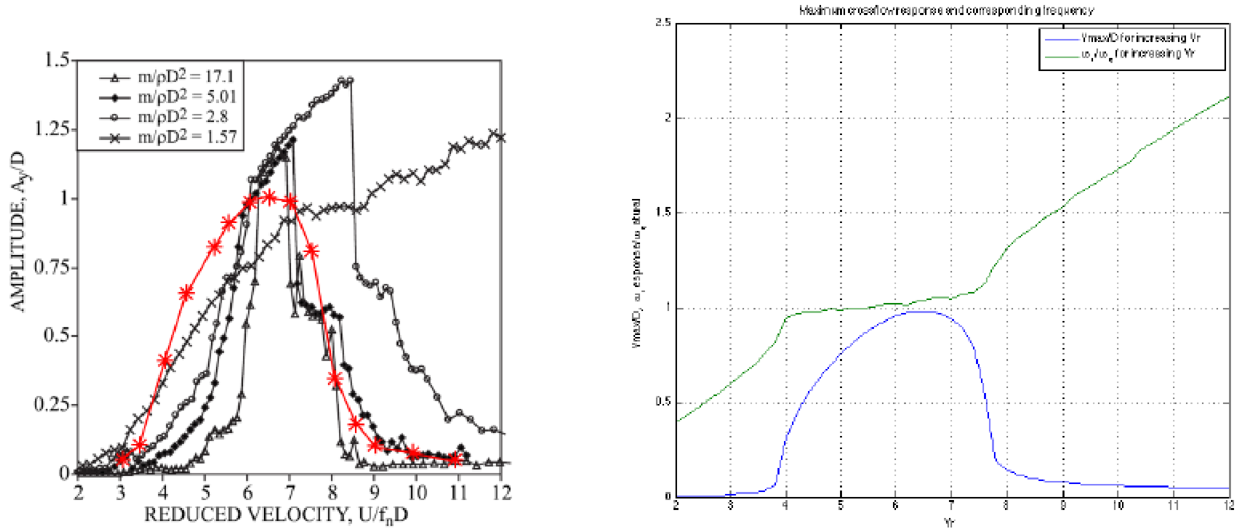

(a) Comparison of vibration amplitudes between model and experiments

(b) $\frac{y}{D}$ and $\frac{\omega_r}{\omega_n}$ in relation to reduced velocity

Figure G.2: Model response for A=10 and ε=0.07 [Slingsby, 2015]

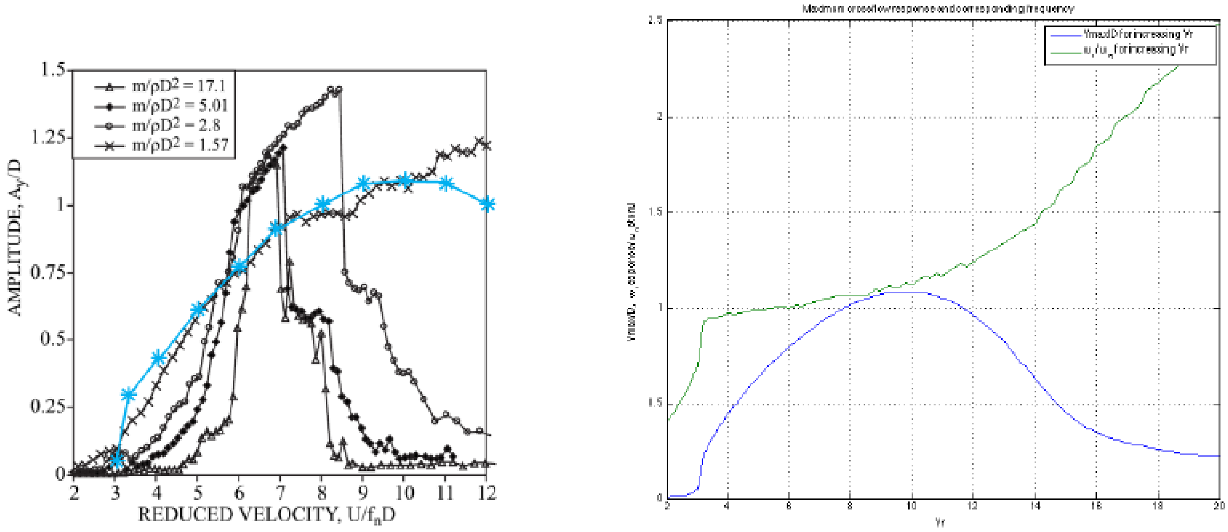

(a) Comparison of vibration amplitudes between model and experiments

(b) $\frac{y}{D}$ and $\frac{\omega_r}{\omega_n}$ in relation to reduced velocity

Figure G.3: Model response for A=19 and ε=0.3 [Slingsby, 2015]

H

OrcaFlex VIV Toolbox

OrcaFlex includes four different time domain VIV models and also offers the option to link to two frequency domain packages by external suppliers (SHEAR, VIVA). The time domain models include two wake oscillator models, namely the Milan Wake Oscillator (Milan WO) and the Iwan & Blevins Wake Oscillator (IBWO) and two vortex tracking models, namely Vortex Tracking model 1 (VT1) and Vortex Tracking model 2 (VT2).

H.1. Validation of VIV models

Against Real world measurements

All OrcaFlex VIV models have been compared with real world test results from three different experiments. Model tank tests conducted at the Delta Flume in Delft [Isherwood, 2007d] DeepStar project test results on Lake Seneca [Isherwood, 2007c] and measurements on a real full scale drilling riser in the Schiehallion field [Isherwood, 2007b]. According to the validation studies of Orcina an important conclusion has been drawn; the Milan model is generally more accurate than the Iwan and Blevins model and both of them are much more accurate than the Vortex tracking models.

Against other VIV software

The results of the laboratory measurements at the Delta Flume in Delft are compared with eleven different numerical models in the paper [Chaplin et al., 2005b]. Among them two numerical models from OrcaFlex were used, namely the Milan model and the Vortex Tracking model 1. The numerical models which were used in the above study can be separated in three groups. The first group (Norsk Hydro, USP, DeepFlow and VIVIC) are Computational Fluid Dynamics based codes and operate in the time domain. CFD techniques are used to calculate the two dimensional flow around the cylinder on a large number of horizontal planes distributed over its length. The second group (Orcina Wake oscillator and Orcina Vortex Tracking) are presented in the following sections. The third group (VIVA, VIVANA, VICoMo, SHEAR7 and ABAVIV) codes operate in the frequency domain. They use data from measurements on rigid cylinders undergoing vortex-induced or forced vibrations to predict the amplitude of the mode/modes which are most likely to be excited. From the results of this publication it is clear that the Milan model of Orcina produces better or equally good results in comparison with the rest of the numerical models.

H.2. Milan Wake Oscillator Model

The Milan model is based on the paper [Falco et al., 1999]. The model is calibrated by assuming a transverse drag coefficient C_{do} equal to 1.2 and a transverse added mass coefficient

C_a equal to 1. The standard Morison drag force in the transverse direction must be added to the force generated by the wake model. So, OrcaFlex calculates the drag forces as usual and then adds the force calculated by the wake model.

The equivalent oscillator is a non-linear one degree of freedom system which transmits to the cable the same force due to the vortex shedding mechanisms. In this model the vortex shedding forces on the nodes are a non-linear function of:

- the fluid velocity
- the displacement and the velocity of the cable node
- the displacement, the velocity and acceleration of the equivalent fluid-dynamic mass represented by the wake oscillator mass M_a.

For a rigid cylinder with mass M_c for an element of the cable, the system can be represented as following:

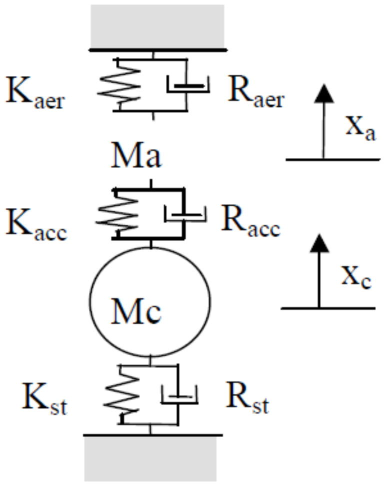

Figure H.1: Equivalent Oscillator

The equations of motion for the system are:

$$\begin{aligned} M_c\ddot{x}_c + R_{st}\dot{x}_c + K_{st}X_c &= -g_{acc}(x_c, x_\alpha, \dot{x}_c, \dot{x}_\alpha, V) \\ M_c\ddot{x}_\alpha &= g_{acc}(x_c, x_\alpha, \dot{x}_c, \dot{x}_\alpha, V) - g_{aer}(x_c, x_\alpha, \dot{x}_c, \dot{x}_\alpha, V) \end{aligned} \tag{H.1}$$

Where the non-linear forces have the following non-linear expressions:

$$\begin{aligned} g_{acc}(x_c, x_\alpha, \dot{x}_c, \dot{x}_\alpha, V) &= K_{Lacc}(x_c - x_\alpha) - K_{NLacc}(x_c - x_\alpha)^3 + R_{Lacc}(\dot{x}_c - \dot{x}_\alpha) - R_{NLacc}(\dot{x}_c - \dot{x}_\alpha)^3 \\ g_{aer}(x_c, x_\alpha, \dot{x}_c, \dot{x}_\alpha, V) &= K_{Laer}x_\alpha - K_{NLaer}(x_\alpha)^3 - R_{Laer}\dot{x}_\alpha + R_{NLaer}(\dot{x}_\alpha)^3 \end{aligned} \tag{H.2}$$

$K_{Lacc} = \frac{1}{2}\rho k1_{acc}DLV^2, \qquad K_{NLacc} = \frac{1}{2}\rho k2_{acc}DLV^2\frac{1}{D^3}$

The equivalent oscillator mass can be evaluated considering that its natural frequency when the cylinder is not vibrating must be related to the Strouhal frequency.

$\omega_s = \sqrt{\frac{K_{Lacc}+K_{Laer}}{M_a}}$

The oscillator parameter values have been obtained by experimental tests.

Table H.1: Equivalent oscillator parameters for smooth cylinders

$k1_{acc}$	1.364	$r1_{acc}$	5.4
$k2_{acc}$	0.2	$r2_{acc}$	0.0
$k1_{aer}$	3.1	$r1_{aer}$	2.15
$k2_{aer}$	0.05	$r2_{aer}$	0.45

H.3. Iwan & Blevins Wake Oscillator Model

This model is based on the paper [Iwan and Blevins, 1974] and uses the Van der Pol equation. The significant difference in comparison with the Milan model is that it includes the standard Morison drag force in the transverse direction. The force exerted on the cylinder by the flow depends only on the velocity and the acceleration of an averaged flow relative to the cylinder and is assumed to be a linear function of the fluid variable z.

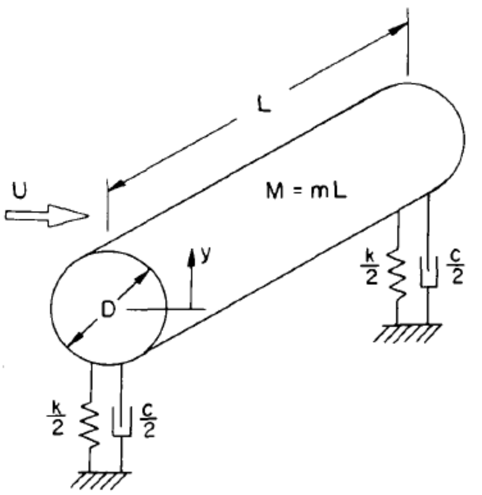

Figure H.2: Elastically supported rigid cylinder

Net force exerted on the cylinder:

$$F_y = a_3 \rho D^2 (\ddot{z} - \ddot{y}) + a_4 \rho D U (\dot{z} - \dot{y}) \tag{H.3}$$

z: the fluid variable

The equations of motion for the system are:

$$\begin{aligned} &\ddot{z} + K' \frac{u_t}{D} \omega_s z = (\alpha_1' - \alpha_4') \frac{U}{D} \dot{z} - a_2' \frac{\dot{z}^3}{UD} + a_3' \ddot{y} + \alpha_4' \frac{U}{D} \dot{y} \\ &\ddot{y} + 2\zeta_T \omega_n \dot{y} + \omega_n^2 y = \alpha_3'' \ddot{z} + \alpha_4'' \dot{z} \frac{U}{D} \end{aligned} \tag{H.4}$$

Where:

$K' = \frac{K}{\alpha_0 + \alpha_3}$, $\quad \alpha_i' = \frac{\alpha_i}{\alpha_0 + \alpha_3}$ $i = 1, 2, 3, 4$, $\quad \alpha_i'' = \frac{\alpha_i \rho D^2}{m + \alpha_3 \rho D^2}$ $i = 3, 4$, $\quad \omega_n = \frac{\sqrt{\frac{k}{m}}}{1 + \frac{\alpha_3 \rho D^2}{m}}$

$\zeta_s = \frac{c}{2\sqrt{km}}$, $\quad \zeta_T = \frac{\zeta_s \frac{\sqrt{\frac{k}{m}}}{\omega_n} + \zeta_f}{1 + \frac{\alpha_3 \rho D^2}{m}}$, $\quad \zeta_f = \frac{\alpha_4 \rho D U}{2 m \omega_n}$, $\quad \omega_s = K' \frac{u_t U}{UD} = 2\pi St \frac{U}{D}$

In which: m is the mass per unit length of the cylinder
k is the support stiffness per unit length
ζ_T is the total effective damping coefficient
ζ_s is the structural viscous damping
ζ_f is the fluid viscous damping

The model parameters have been obtained by experimental data by matching the model response to experimental observations for the cases of fixed cylinder and forced cylinder motion.

Table H.2: Iwan & Blevins model parameters

α_0	α_1	α_2	α_3	α_4
0.48	0.44	0.2	0.0	0.38

H.4. Vortex Tracking Models : VT1 & VT2

These models are based on the physical equations of the boundary layer theory and the Navier–Stokes equation. They are more computationally demanding than the wake oscillator models but much less computationally demanding than CFD models. The Vortex Tracking (2) model is a simplified variant of the Vortex Tracking (1) model is still under development. More information on the vortex tracking models can be found on [Orcina, 2014]. In this thesis the vortex tacking models were not used for the following reasons. Firstly, the according to OrcaFlex's validation the vortex tracking models produce much less accurate results than the wake oscillator models. Secondly, in this thesis a wake oscillator model has been developed and the validation will be made against other models of the same kind.

VIV suppression

The content of this section is confidential

J

VIV guideline

The content of this section is confidential